

Color Image Restoration by Saturation-Value Total Variation*

Zhigang Jia[†], Michael K. Ng[‡], and Wei Wang[§]

Abstract. Color image restoration is one of the important tasks in color image processing. Total variation regularization was proposed and employed for the recovery of edges in a grayscale image. In the literature, there are several methods for extension of total variation regularization for color images, for example, based on color channel coupling and tensor regularization. The main contribution of this paper is to propose and develop a new saturation-value (SV) color total variation regularization in the hue, saturation, and value color space instead of in the original red, green, and blue color space. The development of this SV total variation can be studied via the representation of color images in the quaternion framework for color edge detection. We will investigate the properties of the SV total variation regularization and the resulting optimization model for color image restoration. Numerical examples are presented to demonstrate that the performance of the new SV total variation is better than that of existing color image total variation methods in terms of some criteria such as PSNR, SSIM, and S-CIELAB error.

Key words. color images, total variation, quaternion, color space, regularization, image restoration

AMS subject classifications. 65F22, 68U10, 35A15, 65K10, 52A41

DOI. 10.1137/18M1230451

1. Introduction. Today, color images appear frequently in imaging science. Among various color representation models, RGB (red, green, blue) color space is the most popular one. Many color image processing models are studied based on the RGB color space. In the literature, there are many color spaces for color image processing; see, for instance, [18]. One of the common color spaces is HSV (hue, saturation, value) color space, which is similar to human color perception. The main aim of this paper is to propose a new total variation regularization based on the HSV color space for color image restoration.

Total variation (TV) [30], originally designed for image denoising and restoration for a grayscale image, has become one of the most popular regularization methods in image processing. In the last twenty years, TV has been extended to many other forms for dealing

*Received by the editors December 3, 2018; accepted for publication (in revised form) February 12, 2019; published electronically June 4, 2019.

<http://www.siam.org/journals/siims/12-2/M123045.html>

Funding: The work of the first author was supported in part by the National Natural Science Foundation of China under grant 11771188. The work of the second author was supported in part by the Hong Kong Research Grant Council General Research Fund grants 1202715, 12306616, 12200317, and 12300218 and Hong Kong Baptist University grant RC-ICRS/16-17/03. The work of the third author was supported by the Natural Science Foundation of Shanghai and Fundamental Research Funds for the Central Universities of China grants 22120180255 and 22120180067.

[†]School of Mathematics and Statistics and Jiangsu Key Laboratory of Education Big Data Science and Engineering, Jiangsu Normal University, Xuzhou 221116, People's Republic of China (zhgjia@jsnu.edu.cn).

[‡]Department of Mathematics, Hong Kong Baptist University, Hong Kong (mng@math.hkbu.edu.hk).

[§]Corresponding author. School of Mathematical Sciences, Tongji University, Shanghai, China (wangw@tongji.edu.cn).

with different image processing problems, for instance, anisotropic TV [15], weighted TV [10], fourth-order PDE model [23] (two-step method [24]), higher-order TV [2, 5, 9, 27], or nonlocal TV [16, 36]. On the other hand, TV regularizaton is also extended and studied for vector-valued (color or multichannel) image regularization [1, 3, 4, 6, 8, 12, 21, 22, 26, 29, 33, 37, 38]. In [4], Blomgren and Chan proposed a color TV regularization with a global channel coupling by summing the ℓ^2 norm of each channel TV regularization:

$$(1.1) \quad \text{CTV}_1(\mathbf{u}) := \sqrt{\sum_{k=1}^c \left(\int_{\Omega} \sqrt{(\partial_x u_k(x, y))^2 + (\partial_y u_k(x, y))^2} dx dy \right)^2},$$

where c is the number of channels and $u_k(x, y)$ is the k th channel of vector-valued image $\mathbf{u}(x, y)$ defined on the bounded domain $\Omega \subset \mathbb{R}^2$, i.e., $\mathbf{u}(x, y) = [u_1(x, y), u_2(x, y), \dots, u_c(x, y)]$, and $\partial_x u_k$ (or $\partial_y u_k$) is the partial derivative of u_k with respect to x (or y). In [1, 6, 29, 37], local channel coupling is considered. In particular, Bresson and Chan [6] presented

$$(1.2) \quad \text{CTV}_2(\mathbf{u}) := \int_{\Omega} \sqrt{\sum_{k=1}^c (\partial_x u_k(x, y))^2 + (\partial_y u_k(x, y))^2} dx dy.$$

The main difference between CTV_1 and CTV_2 is their biased classes of functions: uncoupled monotonic functions and channel-coupled monotonic functions, respectively (see [12]). In [12], it is pointed out that CTV_1 is good at color image recovery under similar noise in each channel, and CTV_2 can determine edge locations in different channels while CTV_1 can find out edges and kinks co-located in all the channels. In [12], Duran et al. studied the gradient of a color image as a three dimensional matrix or tensor with dimensions corresponding to the spatial and spectral channels. Different norms along different dimensions can be employed to measure the smoothness of this tensor.

In general, vector-valued images are studied from the view of Riemann geometry. The idea is to study the spectral information of the associated tensor $(\nabla \mathbf{u})^T \nabla \mathbf{u}$ arising from vector-valued images. In [33], Sapiro proposed the following vectorial TV model:

$$\text{VTV}(\mathbf{u}) := \int_{\Omega} S(\lambda((\nabla \mathbf{u}(x, y))^T \nabla \mathbf{u}(x, y))) dx dy,$$

where $(\nabla \mathbf{u}(x, y))^T$ is the transpose of $\nabla \mathbf{u}(x, y)$, $\lambda(\cdot)$ refers to the eigenvalues of $(\nabla \mathbf{u}(x, y))^T \nabla \mathbf{u}(x, y)$, and $S(\cdot)$ is a penalty function on the eigenvalues of $(\nabla \mathbf{u}(x, y))^T \nabla \mathbf{u}(x, y)$. We note that the eigenvalues of $(\nabla \mathbf{u}(x, y))^T \nabla \mathbf{u}(x, y)$ can be used to describe the change of gradient in some directions specified by their eigenvectors. This spectral information would be useful for describing edges of color images. For example, one case is defined by using the Schatten- ∞ norm:

$$(1.3) \quad \text{VTV}_{\text{Schatten}}(\mathbf{u}(x, y)) := \int_{\Omega} \sqrt{\lambda^+(x, y)} dx dy,$$

where $\lambda^+(x, y)$ is the largest eigenvalue of $(\nabla \mathbf{u}(x, y))^T \nabla \mathbf{u}(x, y)$. $\text{VTV}_{\text{Schatten}}(x, y)$ is used to penalize the largest gradient change in $\nabla \mathbf{u}(x, y)$ [17]. Moreover, the Frobenius norm and p -norm can be employed and defined similarly in (1.3); see, for instance, [22]. Other geometric

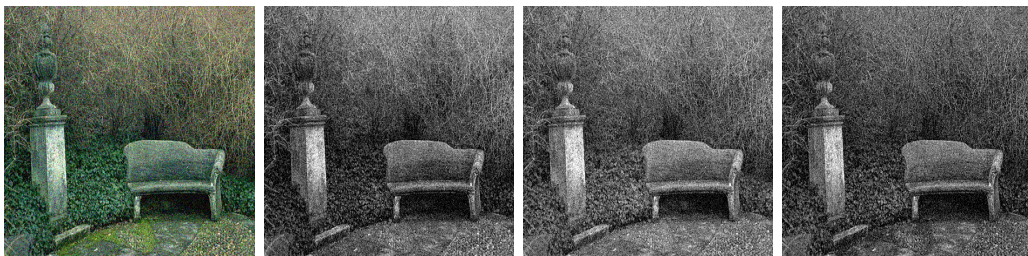


Figure 1. From left to right: the noisy color image; the red channel image; the green channel image; and the blue channel image.

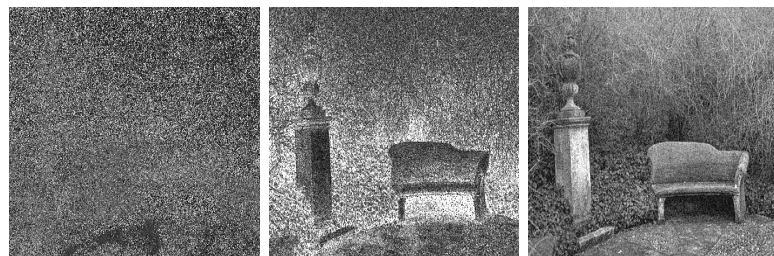


Figure 2. From left to right: the H channel image; the S channel image; and the V channel image.

models are also proposed in the literature. In [21], images were treated as manifolds in a feature-space, and this geometrical interpretation led to a general way for color and color-texture image enhancement. In [3], Bergmann et al. addressed the generalization of the half-quadratic minimization method for image restoration in a Riemannian manifold such as color images.

On the other hand, the transformation of color images between color spaces is a useful technique in color image processing. In [8], Chan, Kang, and Shen studied the TV image restoration based on two nonlinear (or nonflat) color imaging models: the chromaticity-brightness model and the HSV model. After a color image in RGB form is transformed into other color spaces, the TV denoising procedure is applied to the chromaticity component (or the hue component) and the saturation component separately. Their numerical results of color image denoising were shown that the chromaticity TV regularization in the chromaticity-brightness model was better than channel-by-channel TV in RGB and coupled TV CTV₁. The denoising performance of the chromaticity TV regularization is about the same as the hue and saturation TV regularization. Recently, Ono and Yamada [26] considered and used an opponent transformation for decorrelating color images. The vectorial TV regularization is applied to the transformed image and a primal-dual splitting method was developed for solving the resulting optimization model from this color image regularization problem.

The main aim of this paper is to propose and develop a new saturation-value (SV) color TV regularization in the HSV color space for color image restoration instead of in the original RGB color space. In Figure 1, we give a noisy color image and the corresponding RGB channels images. We see that noisy appears in all three color channels. In Figure 2, we also present the same noisy color image in HSV channels. It is interesting to note that the H chan-

nel image does not contain a lot of image details like edges. However, the important color and edge information can be found in the S and V channels images. These results motivate us to develop a TV regularization in S and V channels in the HSV color space. The development of this SV-TV can be studied via the representation of color images in the quaternion framework; see [14, 31, 34] for color edge detection. It is also interesting to note that many color image processing tasks have been developed based on quaternion algebra and analysis, for example, Fourier transform [31], color image compression and enhancement [28], robust color images completion [19], etc. In this paper, we will investigate the properties of the objective function (the combination of the data-fitting term between an unknown color image and observed color image and the SV-TV regularization term) for color image restoration. Numerical examples are presented to demonstrate that the performance of the new SV-TV is better than that of existing color image TV methods in terms of some criteria such as peak signal-to-noise ratio (PSNR), SSIM, and S-CIELAB error.

The outline of this paper is given as follows. In section 2, we review quaternion and the HSV color space. In section 3, we introduce the SV total variation model and discuss the properties of the model. Then we present the iterative algorithm to solve the image restoration model. Based on our framework, we discuss the color image restoration model developed by Ono and Yamada [26] in section 4. In section 5, we report numerical examples to demonstrate our theoretical results. Finally, some concluding remarks are given in section 6.

2. HSV color space and quaternion. The HSV color space is a color system different from the RGB color space and it is usually used for human perception [18]. Hue is the color portion of the color model, expressed as a number from 0 to 360 degrees (color: red, yellow, green, cyan, blue, and magenta). Saturation is the amount of gray in the color. Saturation is expressed in a range from 0 to 1, where 0 is gray and 1 is a primary color. Value works in conjunction with saturation and describes the brightness or intensity of the color, from 0 to 1, where 0 is completely black, and 1 is the brightest and reveals the most color.

Quaternion was introduced by Hamilton [13]. A quaternion function, $\mathbf{u}(x, y)$ from Ω to \mathbb{Q} , is defined as

$$(2.1) \quad \mathbf{u}(x, y) = u_0(x, y) + u_r(x, y)\mathbf{i} + u_g(x, y)\mathbf{j} + u_b(x, y)\mathbf{k},$$

where $(x, y) \in \Omega$, $u_0(x, y)$, $u_r(x, y)$, $u_g(x, y)$, $u_b(x, y) \in \mathbb{R}$ and \mathbf{i} , \mathbf{j} , and \mathbf{k} are three imaginary units satisfying

$$\mathbf{i}^2 = \mathbf{j}^2 = \mathbf{k}^2 = \mathbf{ijk} = -1.$$

For color images, we only have three components, $u_r(x, y)$, $u_g(x, y)$, and $u_b(x, y)$, and $u_0(x, y)$ is always zero. The magnitude of $\mathbf{u}(x, y)$ is defined by

$$|\mathbf{u}(x, y)| = \sqrt{u_0(x, y)^2 + u_r(x, y)^2 + u_g(x, y)^2 + u_b(x, y)^2}.$$

It is interesting to note that HSV components can be expressed by using the operations on

quaternions [11]:

$$(2.2) \quad \begin{cases} c_h(x, y) = \tan^{-1} \left(\frac{|\mathbf{u}(x, y) - \boldsymbol{\mu}\boldsymbol{\nu}\mathbf{u}(x, y)\boldsymbol{\nu}\boldsymbol{\mu}|}{|\mathbf{u}(x, y) - \boldsymbol{\nu}\mathbf{u}(x, y)\boldsymbol{\nu}|} \right), \\ c_s(x, y) = \frac{1}{2}|\mathbf{u}(x, y) + \boldsymbol{\mu}\mathbf{u}(x, y)\boldsymbol{\mu}|, \\ c_v(x, y) = \frac{1}{2}|\mathbf{u}(x, y) - \boldsymbol{\mu}\mathbf{u}(x, y)\boldsymbol{\mu}|, \end{cases}$$

where $\boldsymbol{\mu} = (\mathbf{i} + \mathbf{j} + \mathbf{k})/\sqrt{3}$ referring to the grey-value axis, and $\boldsymbol{\nu}$ is a unit and pure quaternion number and $\boldsymbol{\nu}$ is orthogonal to $\boldsymbol{\mu}$. Note that $\boldsymbol{\mu}^2 = -1$ and $\bar{\boldsymbol{\mu}} = -\boldsymbol{\mu}$. The saturation component $c_s(x, y)$ is the distance between the color vector $\mathbf{u}(x, y)$ at the pixel location (x, y) and the grey axis $\boldsymbol{\mu}$. The value component $c_v(x, y)$ represents the norm of the color vector's orthogonal projection vector $(\mathbf{u}(x, y) \cdot \boldsymbol{\mu})\boldsymbol{\mu}$ on the grey axis $\boldsymbol{\mu}$. The hue component $c_h(x, y)$ is the angle between the color vector $\mathbf{u}(x, y)$ and $\boldsymbol{\mu}$ taken anywhere on the plane orthogonal to $\boldsymbol{\nu}$. The following lemma expresses $c_s(x, y)$ and $c_v(x, y)$ explicitly in terms of $u_r(x, y)$, $u_g(x, y)$, and $u_b(x, y)$.

Lemma 2.1. *Given a color image $\mathbf{u}(x, y) = u_r(x, y)\mathbf{i} + u_g(x, y)\mathbf{j} + u_b(x, y)\mathbf{k}$ (the real component is zero). Then we have*

$$(2.3) \quad c_s(x, y) = \frac{1}{3}\|C\mathbf{u}(x, y)^T\|_2 \quad c_v(x, y) = \frac{1}{\sqrt{3}}|u_r(x, y) + u_g(x, y) + u_b(x, y)|,$$

where

$$\mathbf{C} = \begin{bmatrix} 2 & -1 & -1 \\ -1 & 2 & -1 \\ -1 & -1 & 2 \end{bmatrix}, \quad \mathbf{u}(x, y)^T = \begin{bmatrix} u_r(x, y) \\ u_g(x, y) \\ u_b(x, y) \end{bmatrix},$$

and $\|\cdot\|_2$ is the vector Euclidean norm.

The proof of the above lemma can be obtained by calculation and using the facts that $\mathbf{i}\boldsymbol{\mu} = (-1 + \mathbf{k} - \mathbf{j})/\sqrt{3}$, $\mathbf{j}\boldsymbol{\mu} = (-\mathbf{k} - 1 + \mathbf{i})/\sqrt{3}$, $\mathbf{k}\boldsymbol{\mu} = (\mathbf{j} - \mathbf{i} - 1)/\sqrt{3}$, $\boldsymbol{\mu}\mathbf{i} = (-1 - \mathbf{k} + \mathbf{j})/\sqrt{3}$, $\boldsymbol{\mu}\mathbf{j} = (\mathbf{k} - 1 - \mathbf{i})/\sqrt{3}$, and $\boldsymbol{\mu}\mathbf{k} = (-\mathbf{j} + \mathbf{i} - 1)/\sqrt{3}$.

2.1. Color edge detection. According to the quaternion framework, the edge detection schemes were proposed and developed for color images [11, 32]. It was mentioned in these papers that two different color vectors can have the same hue; it is necessary to use other measures for their difference. Suppose $\mathbf{u}(x, y)$ and $\mathbf{w}(x, y)$ are two given color images using the representation of quaternion:

$$\mathbf{u}(x, y) = u_r(x, y)\mathbf{i} + u_g(x, y)\mathbf{j} + u_b(x, y)\mathbf{k}, \quad \mathbf{w}(x, y) = w_r(x, y)\mathbf{i} + w_g(x, y)\mathbf{j} + w_b(x, y)\mathbf{k}.$$

In [32], Sangwine proposed to use a convolution filter to compute the filtered greyscale value at the pixel location (x, y) based on the distance between the grey axis $\boldsymbol{\mu}$ and $\mathbf{u}(x, y) + \boldsymbol{\mu}\mathbf{w}(x, y)\bar{\boldsymbol{\mu}}$ (the sum of $\mathbf{u}(x, y)$ and the rotated vector $\mathbf{w}(x, y)$). When the filtered value (the corresponding distance) is high, the color opposition is large (i.e., a color edge can be detected). However, it was noted in [11] that false colors are detected in Sangwine's filtering procedure. In [11], Denis, Carre, and Fernandez-Maloigne studied the use of the saturation component

of $\mathbf{u}(x, y) + \mu \mathbf{w}(x, y) \bar{\mu}$ as the distance,

$$(2.4) \quad \begin{aligned} & \frac{1}{2} |(\mathbf{u}(x, y) + \mu \mathbf{w}(x, y) \bar{\mu}) + \mu (\mathbf{u}(x, y) + \mu \mathbf{w}(x, y) \bar{\mu}) \mu| \\ & = \frac{1}{2} |(\mathbf{u}(x, y) - \mathbf{w}(x, y)) + \mu (\mathbf{u}(x, y) - \mathbf{w}(x, y)) \mu|, \end{aligned}$$

i.e., the distance can be measured in the magnitude of the saturation component of $\mathbf{u}(x, y) - \mathbf{w}(x, y)$ (the difference between $\mathbf{u}(x, y)$ and $\mathbf{w}(x, y)$). In [11], the saturation filter was constructed by applying the distance formula in (2.4) only in the horizontal, vertical, and both diagonal directions and the corresponding maximum value at each pixel of the image is selected to be the output filter value for color edge detection. By using (2.3) in Lemma 2.1, we know that the distance can be expressed as follows:

$$(2.5) \quad |\mathbf{u}(x, y) - \mathbf{w}(x, y)|_s := \frac{1}{3} \left\| \mathbf{C} \begin{bmatrix} u_r(x, y) - w_r(x, y) \\ u_g(x, y) - w_g(x, y) \\ u_b(x, y) - w_b(x, y) \end{bmatrix} \right\|_2.$$

Moreover, we can calculate the distance based on the value component of $\mathbf{u}(x, y) - \mathbf{w}(x, y)$:

(2.6)

$$|\mathbf{u}(x, y) - \mathbf{w}(x, y)|_v := \frac{1}{\sqrt{3}} |(u_r(x, y) - w_r(x, y)) + (u_g(x, y) - w_g(x, y)) + (u_b(x, y) - w_b(x, y))|.$$

We remark that if the difference between two color vectors has a high saturation (or value), it seems farther than the difference that has a low saturation (or value) but the same hue. Therefore the distance in hue component is not used in the distance calculation.

3. Saturation-value TV. In view of color edge detection [11], we employ the saturation component to build TV regularization for a color image. Our idea is to make use of neighborhood color pixel values to locate color edges to control regularization in the color image restoration process. In (2.5) and (2.6), we make use of the partial derivatives of $u_r(x, y)$, $u_g(x, y)$, and $u_b(x, y)$ with respect to x (or y) to replace the difference between the two color vectors (i.e., the difference between $\mathbf{u}(x, y)$ and its neighborhood in x - and y -directions). The color image TV regularization for a color image $\mathbf{u}(x, y)$ based on the saturation component is given by

$$(3.1) \quad S\text{-TV}(\mathbf{u}) := \int_{\Omega} \sqrt{|\partial_x \mathbf{u}(x, y)|_s^2 + |\partial_y \mathbf{u}(x, y)|_s^2} dx dy,$$

where

$$(3.2) \quad |\partial_x \mathbf{u}(x, y)|_s = \frac{1}{3} \left\| \mathbf{C} \partial_x \mathbf{u}(x, y)^T \right\|_2, \quad |\partial_y \mathbf{u}(x, y)|_s = \frac{1}{3} \left\| \mathbf{C} \partial_y \mathbf{u}(x, y)^T \right\|_2,$$

$$\partial_x \mathbf{u}(x, y)^T = \begin{bmatrix} \partial_x u_r(x, y) \\ \partial_x u_g(x, y) \\ \partial_x u_b(x, y) \end{bmatrix}, \quad \partial_y \mathbf{u}(x, y)^T = \begin{bmatrix} \partial_y u_r(x, y) \\ \partial_y u_g(x, y) \\ \partial_y u_b(x, y) \end{bmatrix}.$$

We remark that the matrix \mathbf{C} is singular, i.e., when $u_r(x, y) = u_g(x, y) = u_b(x, y)$, $\mathbf{C} \mathbf{u}(x, y)$ is a zero vector. In Figures 3 and 4, we test the proposed color image TV defined in (3.1) to



Figure 3. From left to right: the input image without noise; the edges recovered by using S-TV in (3.1); and SV-TV in (3.3).

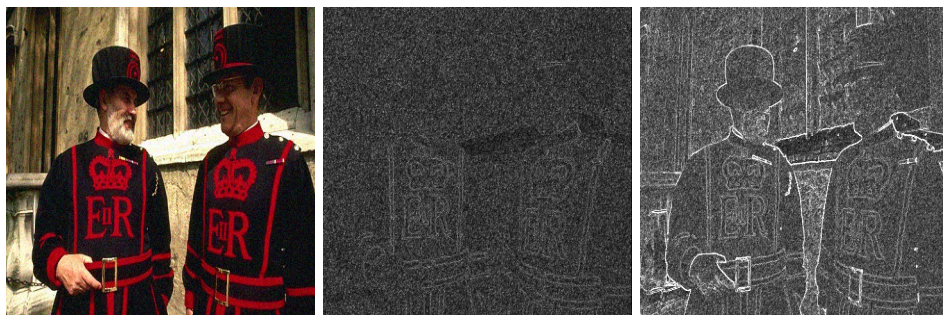


Figure 4. From left to right: the input image with noise; the edges recovered by using S-TV in (3.1); and SV-TV in (3.3).

illustrate its ability of edge detection. According to Figure 3, the edge can be detected quite well when the noise is not present. However, when the input image with Gaussian noise (mean 0 and variance 0.05) is added in each channel, there are many false color edges detected by using (3.1) only (see Figure 4).

In this paper, we further incorporate the value component in (3.1) as the distance to build TV regularization for a color image. More precisely, the color image TV regularization is defined by

$$(3.3) \quad \text{SV-TV}(\mathbf{u}) := \int_{\Omega} \sqrt{|\partial_x \mathbf{u}(x, y)|_s^2 + |\partial_y \mathbf{u}(x, y)|_s^2} + \alpha \sqrt{|\partial_x \mathbf{u}(x, y)|_v^2 + |\partial_y \mathbf{u}(x, y)|_v^2} dx dy,$$

where α is a positive number given as the weight of value component in the TV. In our experimental results, α is just set to be 0.1. We note that

$$(3.4) \quad |\partial_x \mathbf{u}(x, y)|_v = \frac{1}{\sqrt{3}} |\partial_x u_r(x, y) + \partial_x u_g(x, y) + \partial_x u_b(x, y)|$$

and

$$(3.5) \quad |\partial_y \mathbf{u}(x, y)|_v = \frac{1}{\sqrt{3}} |\partial_y u_r(x, y) + \partial_y u_g(x, y) + \partial_y u_b(x, y)|.$$

We see in Figures 3 and 4 that the color edge detection performance by SV-TV is visually better than that by S-TV.

Also we remark that $\text{SV-TV}(\mathbf{u})$ in (3.3) gets the zero value if and only if $\partial_x u_r = \partial_x u_g = \partial_x u_b = 0$ and $\partial_y u_r = \partial_y u_g = \partial_y u_b = 0$. In fact, the function $\text{SV-TV}(\mathbf{u})$ achieves the minimum when

$$\begin{bmatrix} 2 & -1 & -1 \\ -1 & 2 & -1 \\ -1 & -1 & 2 \\ 1 & 1 & 1 \end{bmatrix} \begin{bmatrix} \partial_x u_r & \partial_y u_r \\ \partial_x u_g & \partial_y u_g \\ \partial_x u_b & \partial_y u_b \end{bmatrix} = \begin{bmatrix} 0 & 0 \\ 0 & 0 \\ 0 & 0 \\ 0 & 0 \end{bmatrix}.$$

Since the above coefficient matrix is of full column rank, the above matrix equation has a unique solution. Next we present the dual form and properties of the SV-TV regularization, the SV-TV image restoration model, and the numerical algorithm.

3.1. The dual formulation. In this subsection, we study the dual form of SV-TV. First, we recall the dual form of classical TV [7]. Let \mathbb{B}^m denote the closed unit ball in \mathbb{R}^m with a positive integer m . Let $\mathcal{K}^m = \mathcal{C}^1(\Omega, \mathbb{B}^{2m})$ be the set of continuously differentiable and bounded functions from the compact support in Ω to \mathbb{B}^{2m} . The dual form of the TV of a locally integrable function $u(x, y) \in \mathcal{L}_{\text{loc}}^1(\Omega, \mathbb{R})$ is given by

$$(3.6) \quad \text{TV}(u) := \sup_{\xi \in \mathcal{K}^1} \left\{ \int_{\Omega} u(x, y) \operatorname{div}(\xi(x, y)) dx dy \right\}.$$

When $u(x, y)$ is differentiable,

$$\text{TV}(u) = \int_{\Omega} |\nabla u(x, y)| dx dy.$$

The idea of vectorial TV (see, e.g., [6, 12, 17]) is to extend the above dual form to a vector-valued function $\mathbf{u}(x, y) : \Omega \rightarrow \mathbb{R}^m$. Several dual forms of vectorial TV can be found in [17]. In particular, when we deal with color images ($m = 3$), the dual form of the local channel coupling model CTV₂ [6] in (1.2) is given by

$$(3.7) \quad \text{CTV}_2(\mathbf{u}) = \sup_{(\xi_r, \xi_g, \xi_b) \in \mathcal{K}^3} \left\{ \int_{\Omega} u_r(x, y) \operatorname{div}(\xi_r(x, y)) + u_g(x, y) \operatorname{div}(\xi_g(x, y)) + u_b(x, y) \operatorname{div}(\xi_b(x, y)) dx dy \right\}.$$

Based on above listed dual forms, we can derive the dual form of SV-TV.

Proposition 3.1. *Suppose $\mathbf{u}(x, y)$ is differentiable. Then $\text{SV-TV}(\mathbf{u})$ is given by*

$$(3.8) \quad \begin{aligned} & \sup_{(\xi_1, \xi_2, \xi_3) \in \mathcal{K}^2, \xi_3 \in \mathcal{K}^1} \left\{ \int_{\Omega} \frac{1}{\sqrt{2}}(u_r(x, y) - u_g(x, y)) \operatorname{div}(\xi_1(x, y)) \right. \\ & \quad + \frac{1}{\sqrt{6}}(u_r(x, y) + u_g(x, y) - 2u_b(x, y)) \operatorname{div}(\xi_2(x, y)) \\ & \quad \left. + \frac{\alpha}{\sqrt{3}}(u_r(x, y) + u_g(x, y) + u_b(x, y)) \operatorname{div}(\xi_3(x, y)) dx dy \right\}. \end{aligned}$$

Proof. We first set

$$(3.9) \quad \begin{bmatrix} \phi_1(x, y) \\ \phi_2(x, y) \\ \phi_3(x, y) \end{bmatrix} = \mathbf{P} \begin{bmatrix} u_r(x, y) \\ u_g(x, y) \\ u_b(x, y) \end{bmatrix},$$

where \mathbf{P} is an orthogonal matrix given by

$$(3.10) \quad \mathbf{P} = \begin{bmatrix} \frac{1}{\sqrt{2}} & \frac{-1}{\sqrt{2}} & 0 \\ \frac{1}{\sqrt{6}} & \frac{1}{\sqrt{6}} & -\frac{2}{\sqrt{6}} \\ \frac{1}{\sqrt{3}} & \frac{1}{\sqrt{3}} & \frac{1}{\sqrt{3}} \end{bmatrix}.$$

Recalling that $u_r(x, y)$, $u_g(x, y)$, and $u_b(x, y)$ are differential, so are $\phi_1(x, y)$, $\phi_2(x, y)$, and $\phi_3(x, y)$. Then the dual form in (3.8) can be rewritten as

$$\begin{aligned} & \sup_{(\xi_1, \xi_2) \in \mathcal{K}^2} \left\{ \int_{\Omega} \phi_1(x, y) \operatorname{div}(\xi_1(x, y)) + \phi_2(x, y) \operatorname{div}(\xi_2(x, y)) dx dy \right\} \\ & \quad + \alpha \sup_{\xi_3 \in \mathcal{K}^1} \left\{ \int_{\Omega} \phi_3(x, y) \operatorname{div}(\xi_3(x, y)) dx dy \right\} \\ &= \int_{\Omega} \sqrt{\sum_{k=1}^2 (\partial_x \phi_k(x, y))^2 + (\partial_y \phi_k(x, y))^2} dx dy + \alpha \int_{\Omega} \sqrt{(\partial_x \phi_3(x, y))^2 + (\partial_y \phi_3(x, y))^2} dx dy. \end{aligned} \quad (3.11)$$

By using (3.4) and (3.5), the second term of (3.11) is equal to

$$\begin{aligned} & \frac{\alpha}{\sqrt{3}} \int_{\Omega} \sqrt{(\sqrt{3} \partial_x \phi_3(x, y))^2 + (\sqrt{3} \partial_y \phi_3(x, y))^2} dx dy \\ &= \frac{\alpha}{\sqrt{3}} \int_{\Omega} \sqrt{|\partial_x u_r(x, y) + \partial_x u_g(x, y) + \partial_x u_b(x, y)|^2 + |\partial_y u_r(x, y) + \partial_y u_g(x, y) + \partial_y u_b(x, y)|^2} dx dy \\ &= \alpha \int_{\Omega} \sqrt{|\partial_x \mathbf{u}(x, y)|_v^2 + |\partial_y \mathbf{u}(x, y)|_v^2} dx dy. \end{aligned}$$

Noting that

$$(3.12) \quad \mathbf{C} = \mathbf{P}^T \begin{bmatrix} 3 & 0 & 0 \\ 0 & 3 & 0 \\ 0 & 0 & 0 \end{bmatrix} \mathbf{P},$$

where \mathbf{C} is defined in Lemma 2.1, we deduce that the first term of (3.11) is equivalent to

$$\begin{aligned}
& \frac{1}{3} \int_{\Omega} \sqrt{\left\| \begin{bmatrix} 3 & 0 & 0 \\ 0 & 3 & 0 \\ 0 & 0 & 0 \end{bmatrix} \begin{bmatrix} \partial_x \phi_1(x, y) \\ \partial_x \phi_2(x, y) \\ \partial_x \phi_3(x, y) \end{bmatrix} \right\|_2^2 + \left\| \begin{bmatrix} 3 & 0 & 0 \\ 0 & 3 & 0 \\ 0 & 0 & 0 \end{bmatrix} \begin{bmatrix} \partial_y \phi_1(x, y) \\ \partial_y \phi_2(x, y) \\ \partial_y \phi_3(x, y) \end{bmatrix} \right\|_2^2} dxdy \\
&= \frac{1}{3} \int_{\Omega} \sqrt{\left\| \mathbf{P}^T \begin{bmatrix} 3 & 0 & 0 \\ 0 & 3 & 0 \\ 0 & 0 & 0 \end{bmatrix} \mathbf{P} \mathbf{P}^T \begin{bmatrix} \partial_x \phi_1(x, y) \\ \partial_x \phi_2(x, y) \\ \partial_x \phi_3(x, y) \end{bmatrix} \right\|_2^2 + \left\| \mathbf{P}^T \begin{bmatrix} 3 & 0 & 0 \\ 0 & 3 & 0 \\ 0 & 0 & 0 \end{bmatrix} \mathbf{P} \mathbf{P}^T \begin{bmatrix} \partial_y \phi_1(x, y) \\ \partial_y \phi_2(x, y) \\ \partial_y \phi_3(x, y) \end{bmatrix} \right\|_2^2} dxdy \\
&= \frac{1}{3} \int_{\Omega} \sqrt{\left\| \mathbf{C} \begin{bmatrix} \partial_x u_r(x, y) \\ \partial_x u_g(x, y) \\ \partial_x u_b(x, y) \end{bmatrix} \right\|_2^2 + \left\| \mathbf{C} \begin{bmatrix} \partial_y u_r(x, y) \\ \partial_y u_g(x, y) \\ \partial_y u_b(x, y) \end{bmatrix} \right\|_2^2} dxdy \\
&= \int_{\Omega} \sqrt{|\partial_x \mathbf{u}(x, y)|_s^2 + |\partial_y \mathbf{u}(x, y)|_s^2} dxdy.
\end{aligned}$$

The result follows. ■

The following convexity, lower semicontinuity, approximation, and compactness properties can be established based on the dual form of SV-TV; see [6, 7, 17] for similar results of classic TV and vectorial TV.

Proposition 3.2. (i) $\text{SV-TV}(\mathbf{u})$ in (3.8) is a convex function with respect to $\mathbf{u}(x, y)$.

(ii) Let $\mathbf{u}^{(n)}(x, y) = [u_r^{(n)}(x, y), u_g^{(n)}(x, y), u_b^{(n)}(x, y)]$, $\mathbf{u}(x, y) = [u_r(x, y), u_g(x, y), u_b(x, y)]$. Assume that $u_r^{(n)}(x, y), u_g^{(n)}(x, y), u_b^{(n)}(x, y) \in BV(\Omega)$, and $u_r^{(n)}(x, y) \rightarrow u_r(x, y)$, $u_g^{(n)}(x, y) \rightarrow u_g(x, y)$, $u_b^{(n)}(x, y) \rightarrow u_b(x, y)$ in $L^1(\Omega)$, and then

$$\liminf_{n \rightarrow \infty} \text{SV-TV}(\mathbf{u}^{(n)}) \geq \text{SV-TV}(\mathbf{u}).$$

(iii) For any $\mathbf{u} = [u_r(x, y), u_g(x, y), u_b(x, y)]$ with $u_r(x, y), u_g(x, y), u_b(x, y) \in BV(\Omega)$, there exists a sequence $\{\mathbf{u}^{(n)}(x, y) = [u_r^{(n)}(x, y), u_g^{(n)}(x, y), u_b^{(n)}(x, y)]\}$ with $\{u_r^{(n)}(x, y)\}$, $\{u_g^{(n)}(x, y)\}$, $\{u_b^{(n)}(x, y)\} \subset C^\infty(\Omega) \cap W^{1,1}(\Omega)$ such that

$$\lim_{n \rightarrow \infty} \int_{\Omega} |u_r^{(n)}(x, y) - u_r(x, y)| dxdy = 0, \quad \lim_{n \rightarrow \infty} \int_{\Omega} |u_g^{(n)}(x, y) - u_g(x, y)| dxdy = 0,$$

$$\lim_{n \rightarrow \infty} \int_{\Omega} |u_b^{(n)}(x, y) - u_b(x, y)| dxdy = 0, \quad \lim_{n \rightarrow \infty} \text{SV-TV}(\mathbf{u}^{(n)}) = \text{SV-TV}(\mathbf{u}).$$

(iv) Assume $\{\text{SV-TV}(\mathbf{u}^{(n)}) + \|u_r^{(n)}(x, y)\|_{L^1} + \|u_g^{(n)}(x, y)\|_{L^1} + \|u_b^{(n)}(x, y)\|_{L^1}\}$ is uniformly bounded, and then there exist a subsequence ($\{\mathbf{u}^{(n)}(x, y) = [u_r^{(n)}(x, y), u_g^{(n)}(x, y), u_b^{(n)}(x, y)]\}$) and $u_r(x, y), u_g(x, y), u_b(x, y) \in BV(\Omega)$ such that

$$u_r^{(n)}(x, y) \rightarrow u_r(x, y), \quad u_g^{(n)}(x, y) \rightarrow u_g(x, y), \quad u_b^{(n)}(x, y) \rightarrow u_b(x, y) \text{ in } L^1(\Omega).$$

3.2. Color image restoration model. In this subsection, we study the following SV-TV color image restoration model:

$$(3.13) \quad \min_{u_r(x,y), u_g(x,y), u_b(x,y) \in \mathbb{BV}(\Omega)} \left\{ \text{SV-TV}(\mathbf{u}) + \frac{\lambda}{2} \int_{\Omega} |(K \star \mathbf{u})(x,y) - \mathbf{z}(x,y)|^2 dx dy \right\},$$

where K is a given blurring operator, \star is the convolution operation, and $\lambda > 0$ is a positive regularization parameter. The next theorem states the existence and uniqueness of the solution of (3.13).

Theorem 3.3. *The minimization problem (3.13) has at least one solution. If $\mathbf{u}(x,y) \mapsto (K \star \mathbf{u})(x,y)$ is injective, the solution is unique.*

Proof. We choose $\mathbf{u}(x,y)$ to be constant, and then the energy in (3.13) is finite. This implies that the infimum of the energy must be finite. Suppose $\{\mathbf{u}^{(n)}(x,y)\}$ is a minimizing sequence of problem (3.13). Then there exists a constant $M > 0$ such that

$$\text{SV-TV}(\mathbf{u}^{(n)}) \leq M.$$

By combining them with the boundedness of $u_r^{(n)}(x,y)$, $u_g^{(n)}(x,y)$, $u_b^{(n)}(x,y)$, we get that $\{\text{SV-TV}(\mathbf{u}^n) + \sum_{i=r,g,b} \|u_i^{(n)}(x,y)\|_{L^1}\}$ is uniformly bounded. Noting the compactness property of Proposition 3.2, up to a subsequence also denoted by $\{u_r^{(n)}(x,y), u_g^{(n)}(x,y), u_b^{(n)}(x,y)\}$, there exist $u_r^*(x,y)$, $u_g^*(x,y)$, $u_b^*(x,y) \in BV(\Omega)$ such that

$$u_r^{(n)}(x,y) \xrightarrow{L^1(\Omega)} u_r^*(x,y), \quad u_r^{(n)}(x,y) \rightarrow u_r^*(x,y) \quad \text{a.e. } (x,y) \in \Omega,$$

$$u_g^{(n)}(x,y) \xrightarrow{L^1(\Omega)} u_g^*(x,y), \quad u_g^{(n)}(x,y) \rightarrow u_g^*(x,y) \quad \text{a.e. } (x,y) \in \Omega,$$

and

$$u_b^{(n)}(x,y) \xrightarrow{L^1(\Omega)} u_b^*(x,y), \quad u_b^{(n)}(x,y) \rightarrow u_b^*(x,y) \quad \text{a.e. } (x,y) \in \Omega.$$

As a consequence of the lower semicontinuity of $\text{SV-TV}(\mathbf{u})$,

$$(3.14) \quad \liminf \text{SV-TV}(\mathbf{u}^{(n)}) \geq \text{SV-TV}(\mathbf{u}^*).$$

Meanwhile, the following convergence results hold:

$$((K \star u_r^{(n)})(x,y) - z_r(x,y))^2 \rightarrow ((K \star u_r^*)(x,y) - z_r(x,y))^2 \quad \text{a.e. } (x,y) \in \Omega,$$

$$((K \star u_g^{(n)})(x,y) - z_g(x,y))^2 \rightarrow ((K \star u_g^*)(x,y) - z_g(x,y))^2 \quad \text{a.e. } (x,y) \in \Omega,$$

and

$$((K \star u_b^{(n)})(x,y) - z_b(x,y))^2 \rightarrow ((K \star u_b^*)(x,y) - z_b(x,y))^2 \quad \text{a.e. } (x,y) \in \Omega.$$

By using Fatou's lemma, we have

$$\begin{aligned}
 & \liminf \int_{\Omega} ((K \star u_r^{(n)})(x, y) - z_r(x, y))^2 dx dy + \int_{\Omega} ((K \star u_g^{(n)})(x, y) - z_g(x, y))^2 dx dy \\
 & \quad + \int_{\Omega} ((K \star u_b^{(n)})(x, y) - z_b(x, y))^2 dx dy \\
 & \geq \int_{\Omega} ((K \star u_r^*)(x, y) - z_r(x, y))^2 dx dy + \int_{\Omega} ((K \star u_g^*)(x, y) - z_g(x, y))^2 dx dy \\
 & \quad + \int_{\Omega} ((K \star u_b^*)(x, y) - z_b(x, y))^2 dx dy. \tag{3.15}
 \end{aligned}$$

By noting the lower semicontinuity in (3.14) and (3.15), we obtain

$$\begin{aligned}
 & \liminf \text{SV-TV}(\mathbf{u}^{(n)}) + \int_{\Omega} ((K \star u_r^{(n)})(x, y) - z_r(x, y))^2 dx dy \\
 & \quad + \int_{\Omega} ((K \star u_g^{(n)})(x, y) - z_g(x, y))^2 dx dy + \int_{\Omega} ((K \star u_b^{(n)})(x, y) - z_b(x, y))^2 dx dy \\
 & \geq \text{SV-TV}(\mathbf{u}^*(x, y)) + \int_{\Omega} ((K \star u_r^*)(x, y) - z_r(x, y))^2 dx dy \\
 & \quad + \int_{\Omega} ((K \star u_g^*)(x, y) - z_g(x, y))^2 dx dy + \int_{\Omega} ((K \star u_b^*)(x, y) - z_b(x, y))^2 dx dy.
 \end{aligned}$$

It leads to the existence of the solution of (3.13). It is clear that if $\mathbf{u}(x, y) \mapsto (K \star \mathbf{u})(x, y)$ is injective, it follows the strict convexity of the functional which guarantees the uniqueness of the solution. \blacksquare

On the other hand, the Euler–Lagrange equation of the SV-TV model (3.13) is

$$\begin{aligned}
 & \nabla \cdot \left(\frac{\nabla(2u_r - u_g - u_b)(x, y)}{\sqrt{|\partial_x \mathbf{u}(x, y)|_s^2 + |\partial_y \mathbf{u}(x, y)|_s^2}} + \alpha \frac{\nabla(u_r + u_g + u_b)(x, y)}{\sqrt{|\partial_x \mathbf{u}(x, y)|_v^2 + |\partial_y \mathbf{u}(x, y)|_v^2}} \right) \\
 & \quad - 3\lambda((K^* \star K \star u_r)(x, y) - (K^* \star z_r)(x, y)) = 0, \\
 & \nabla \cdot \left(\frac{\nabla(2u_g - u_b - u_r)(x, y)}{\sqrt{|\partial_x \mathbf{u}(x, y)|_s^2 + |\partial_y \mathbf{u}(x, y)|_s^2}} + \alpha \frac{\nabla(u_r + u_g + u_b)(x, y)}{\sqrt{|\partial_x \mathbf{u}(x, y)|_v^2 + |\partial_y \mathbf{u}(x, y)|_v^2}} \right) \\
 & \quad - 3\lambda((K^* \star K \star u_g)(x, y) - (K^* \star z_g)(x, y)) = 0, \\
 & \nabla \cdot \left(\frac{\nabla(2u_b - u_r - u_g)(x, y)}{\sqrt{|\partial_x \mathbf{u}(x, y)|_s^2 + |\partial_y \mathbf{u}(x, y)|_s^2}} + \alpha \frac{\nabla(u_r + u_g + u_b)(x, y)}{\sqrt{|\partial_x \mathbf{u}(x, y)|_v^2 + |\partial_y \mathbf{u}(x, y)|_v^2}} \right) \\
 & \quad - 3\lambda((K^* \star K \star u_b)(x, y) - (K^* \star z_b)(x, y)) = 0, \tag{3.16}
 \end{aligned}$$

where K^* is the conjugate transpose of K . As a comparison, we list the Euler–Lagrange

equations of CTV₁ [4] in (1.1) and CTV₂ [6] in (1.2), respectively, as follows:

$$\begin{aligned} \frac{TV(u_r(x,y))}{CTV_1(\mathbf{u}(x,y))} \nabla \cdot \left(\frac{\nabla u_r(x,y)}{|\nabla u_r(x,y)|} \right) - \lambda((K^* \star K \star u_c)(x,y) - (K^* \star z_c)(x,y)) &= 0, \\ \frac{TV(u_g(x,y))}{CTV_1(\mathbf{u}(x,y))} \nabla \cdot \left(\frac{\nabla u_g(x,y)}{|\nabla u_g(x,y)|} \right) - \lambda((K^* \star K \star u_g)(x,y) - (K^* \star z_g)(x,y)) &= 0, \\ \frac{TV(u_b(x,y))}{CTV_1(\mathbf{u}(x,y))} \nabla \cdot \left(\frac{\nabla u_b(x,y)}{|\nabla u_b(x,y)|} \right) - \lambda((K^* \star K \star u_b)(x,y) - (K^* \star z_b)(x,y)) &= 0, \end{aligned}$$

and

$$\begin{aligned} \nabla \cdot \left(\frac{\nabla u_r(x,y)}{|\mathbf{u}(x,y)|} \right) + \nabla \cdot \left(\frac{\nabla u_g(x,y)}{|\mathbf{u}(x,y)|} \right) + \nabla \cdot \left(\frac{\nabla u_b(x,y)}{|\mathbf{u}(x,y)|} \right) - \lambda((K^* \star K \star u_r)(x,y) \\ - (K^* \star z_r)(x,y)) - \lambda((K^* \star K \star u_g)(x,y) - (K^* \star z_g)(x,y)) - \lambda((K^* \star K \star u_b)(x,y) \\ - (K^* \star z_b)(x,y)) = 0. \end{aligned} \quad (3.17)$$

By comparing (3.16) and (3.17), we see that SV-TV takes the form of coupling channelwise diffusion coefficients in the saturation component, $\sqrt{|\partial_x \mathbf{u}(x,y)|_s^2 + |\partial_y \mathbf{u}(x,y)|_s^2}$, and in value component, $\sqrt{|\partial_x \mathbf{u}(x,y)|_v^2 + |\partial_y \mathbf{u}(x,y)|_v^2}$, while CTV₁ takes the form of the individual channel diffusion coefficient only in $|\nabla u_c(x,y)|$, where $c = r, g$, or b . In contrast, the global channelwise scaling factor $\frac{TV(u_c(x,y))}{CTV_1(\mathbf{u}(x,y))}$ is multiplied in the diffusion term $\nabla \cdot (\frac{\nabla u_c(x,y)}{|\nabla u_c(x,y)|})$ for $c = r, g, b$. Again by comparing (3.16) and (3.17), we see that SV-TV takes the form of three diffusion equations corresponding to three color channels, and each diffusion equation still involves three color channel variables, while CTV₂ takes the form of only one diffusion equation by combining the RGB channels together: $\nabla \cdot (\frac{\nabla u_r(x,y)}{|\mathbf{u}(x,y)|}) + \nabla \cdot (\frac{\nabla u_g(x,y)}{|\mathbf{u}(x,y)|}) + \nabla \cdot (\frac{\nabla u_b(x,y)}{|\mathbf{u}(x,y)|})$. Because of coupling among three color channels in diffusion coefficients and equations, we expect that the color image restoration may be enhanced. In section 5, numerical examples are given to demonstrate the effectiveness of the proposed model.

3.3. Numerical algorithm. In this subsection, we first present the discrete version of the SV-TV model (3.13). Two discrete differential operators \mathbf{D}_x and \mathbf{D}_y are defined as follows:

$$(\mathbf{D}_x \mathbf{u})_{ij} = \mathbf{u}(i,j) - \mathbf{u}(i-1,j), \quad (\mathbf{D}_y \mathbf{u})_{ij} = \mathbf{u}(i,j) - \mathbf{u}(i,j-1).$$

We always assume proper boundary conditions. For example, $\mathbf{u}_{i,j} = 0$ if $i = 0$ or $m + 1$ or $j = 0$ or $n + 1$ under the zero boundary condition. Then the discrete SV-TV corresponding to (3.3) is defined as follows:

$$(3.18) \quad \text{SV-TV}(\mathbf{u}) = \sum_{i=1}^m \sum_{j=1}^n \left(\sqrt{|(\mathbf{D}_x \mathbf{u})_{ij}|_s^2 + |(\mathbf{D}_y \mathbf{u})_{ij}|_s^2} + \alpha \sqrt{|(\mathbf{D}_x \mathbf{u})_{ij}|_v^2 + |(\mathbf{D}_y \mathbf{u})_{ij}|_v^2} \right),$$

where m and n are the number of pixels in the horizontal and vertical directions of the discretized image.

Next we develop an efficient optimization algorithm to solve the discretized version of (3.13). The main idea is to transform the variables suitably so that the classical ADMM

algorithm can be applied directly. The transformation in (3.9) and (3.10) can be applied to the discrete variables \mathbf{u}_r , \mathbf{u}_g , and \mathbf{u}_b . In particular,

$$\mathbf{q} = \begin{bmatrix} \mathbf{q}_1 \\ \mathbf{q}_2 \\ \mathbf{q}_3 \end{bmatrix} = \mathbf{P} \begin{bmatrix} \mathbf{u}_r \\ \mathbf{u}_g \\ \mathbf{u}_b \end{bmatrix},$$

where

$$(3.19) \quad \mathbf{P} = \begin{bmatrix} \frac{1}{\sqrt{2}}\mathbf{I} & \frac{-1}{\sqrt{2}}\mathbf{I} & \mathbf{0} \\ \frac{1}{\sqrt{6}}\mathbf{I} & \frac{1}{\sqrt{6}}\mathbf{I} & -\frac{2}{\sqrt{6}}\mathbf{I} \\ \frac{1}{\sqrt{3}}\mathbf{I} & \frac{1}{\sqrt{3}}\mathbf{I} & \frac{1}{\sqrt{3}}\mathbf{I} \end{bmatrix}.$$

Let \mathbf{K} denote the discrete form of the blurring operator. Because of the transformation \mathbf{P} , we consider the transformed blurring operator, $\tilde{\mathbf{K}} = \mathbf{PKP}^T$, and the transformed observed image, $\tilde{\mathbf{z}} = \mathbf{Pz}$. Then the discrete version of SV-TV color image restoration model (3.13) is given by

$$(3.20) \quad \min_{\mathbf{q}} \sum_{i=1}^m \sum_{j=1}^n \left(\sqrt{(\mathbf{D}_x \mathbf{q}_1)_{ij}^2 + (\mathbf{D}_x \mathbf{q}_2)_{ij}^2 + (\mathbf{D}_y \mathbf{q}_1)_{ij}^2 + (\mathbf{D}_y \mathbf{q}_2)_{ij}^2} \right. \\ \left. + \alpha \sqrt{(\mathbf{D}_x \mathbf{q}_3)_{ij}^2 + (\mathbf{D}_y \mathbf{q}_3)_{ij}^2} \right) + \frac{\lambda}{2} \|\tilde{\mathbf{K}}\mathbf{q} - \tilde{\mathbf{z}}\|_2^2.$$

Then we introduce auxiliary variables $\mathbf{w}_1^x, \mathbf{w}_2^x, \mathbf{w}_3^x, \mathbf{w}_1^y, \mathbf{w}_2^y$, and \mathbf{w}_3^y and rewrite (3.20) into the following equivalent constrained minimization problem:

$$\min_{\mathbf{q}} \sum_{i=1}^m \sum_{j=1}^n \left(\sqrt{|(\mathbf{w}_1^x)_{ij}|^2 + |(\mathbf{w}_2^x)_{ij}|^2 + |(\mathbf{w}_1^y)_{ij}|^2 + |(\mathbf{w}_2^y)_{ij}|^2} \right. \\ \left. + \alpha \sqrt{|(\mathbf{w}_3^x)_{ij}|^2 + |(\mathbf{w}_3^y)_{ij}|^2} \right) + \frac{\lambda}{2} \|\tilde{\mathbf{K}}\mathbf{q} - \tilde{\mathbf{z}}\|_2^2$$

subject to $\mathbf{w}_1^x = \mathbf{D}_x \mathbf{q}_1, \mathbf{w}_2^x = \mathbf{D}_x \mathbf{q}_2, \mathbf{w}_3^x = \mathbf{D}_x \mathbf{q}_3, \mathbf{w}_1^y = \mathbf{D}_y \mathbf{q}_1, \mathbf{w}_2^y = \mathbf{D}_y \mathbf{q}_2, \mathbf{w}_3^y = \mathbf{D}_y \mathbf{q}_3$.

By introducing Lagrangian multipliers τ_j^x and τ_j^y ($j = 1, 2, 3$) and a penalty parameter $\beta > 0$, we derive the augmented Lagrangian of the above minimization problem,

$$\sum_{i=1}^m \sum_{j=1}^n \left(\sqrt{|(\mathbf{w}_1^x)_{ij}|^2 + |(\mathbf{w}_2^x)_{ij}|^2 + |(\mathbf{w}_1^y)_{ij}|^2 + |(\mathbf{w}_2^y)_{ij}|^2} + \alpha \sqrt{|(\mathbf{w}_3^x)_{ij}|^2 + |(\mathbf{w}_3^y)_{ij}|^2} \right) \\ + \frac{\lambda}{2} \|\tilde{\mathbf{K}}\mathbf{q} - \tilde{\mathbf{z}}\|_2^2 + (\tau_1^x, \mathbf{w}_1^x - \mathbf{D}_x \mathbf{q}_1) + (\tau_2^x, \mathbf{w}_2^x - \mathbf{D}_x \mathbf{q}_2) + (\tau_3^x, \mathbf{w}_3^x - \mathbf{D}_x \mathbf{q}_3) \\ + (\tau_1^y, \mathbf{w}_1^y - \mathbf{D}_y \mathbf{q}_1) + (\tau_2^y, \mathbf{w}_2^y - \mathbf{D}_y \mathbf{q}_2) + (\tau_3^y, \mathbf{w}_3^y - \mathbf{D}_y \mathbf{q}_3) + \frac{\beta}{2} \left(\|\mathbf{w}_1^x - \mathbf{D}_x \mathbf{q}_1\|^2 \right. \\ \left. + \|\mathbf{w}_2^x - \mathbf{D}_x \mathbf{q}_2\|^2 + \|\mathbf{w}_3^x - \mathbf{D}_x \mathbf{q}_3\|^2 + \|\mathbf{w}_1^y - \mathbf{D}_y \mathbf{q}_1\|^2 + \|\mathbf{w}_2^y - \mathbf{D}_y \mathbf{q}_2\|^2 + \|\mathbf{w}_3^y - \mathbf{D}_y \mathbf{q}_3\|^2 \right).$$

Then ADMM iteration can be applied to solve the above optimization problem. In the practical implementation, we gather the variables together and compute them in parallel. Indeed, it is two-step scheme of the ADMM iteration. We note that the closed-form solutions of such ADMM iteration can be obtained efficiently by using fast Fourier transforms and soft-thresholding operation. Another efficient method, the dual method, has been studied in [38] and can be applied to solve the proposed optimization problem.

4. The DTV model. Recently, Ono and Yamada [26] considered and used an opponent transformation for decorrelating color images as follows:

$$(4.1) \quad \begin{bmatrix} f_1(x, y) \\ f_2(x, y) \\ f_3(x, y) \end{bmatrix} = \mathbf{F} \begin{bmatrix} u_r(x, y) \\ u_g(x, y) \\ u_b(x, y) \end{bmatrix},$$

where \mathbf{F} is an orthogonal matrix given by

$$(4.2) \quad \mathbf{F} = \begin{bmatrix} \frac{1}{\sqrt{2}} & 0 & \frac{-1}{\sqrt{2}} \\ \frac{1}{\sqrt{6}} & -\frac{2}{\sqrt{6}} & \frac{1}{\sqrt{6}} \\ \frac{1}{\sqrt{3}} & \frac{1}{\sqrt{3}} & \frac{1}{\sqrt{3}} \end{bmatrix}.$$

By comparing (3.10) and (4.2), it's clear that \mathbf{P} is different from \mathbf{F} , but they are very close except on how to use blue and green channels in the transformation. More precisely, the difference between red and blue channels is the first output $f_1(x, y)$ and the difference between $u_r(x, y) - u_g(x, y)$ and $u_g(x, y) - u_b(x, y)$ is the second output $f_2(x, y)$. In the proposed model, the difference between red and green channels and the difference between $u_r(x, y) - u_b(x, y)$ and $u_b(x, y) - u_g(x, y)$ are employed. Since C has two eigenvalues having the same value of 3, we can obtain

$$\mathbf{C} = \mathbf{F}^T \begin{bmatrix} 3 & 0 & 0 \\ 0 & 3 & 0 \\ 0 & 0 & 0 \end{bmatrix} \mathbf{F}$$

instead of (3.12). Because of the similarity between the proposed model and the DTV model, the dual form of DTV(\mathbf{u}) is given by

$$(4.3) \quad \begin{aligned} & \sup_{(\xi_1, \xi_2) \in \mathcal{K}^2, \xi_3 \in \mathcal{K}^1} \left\{ \int_{\Omega} \frac{1}{\sqrt{2}} (u_r(x, y) - u_b(x, y)) \operatorname{div} (\xi_1(x, y)) \right. \\ & \quad + \frac{1}{\sqrt{6}} (u_r(x, y) - 2u_g(x, y) + u_b(x, y)) \operatorname{div} (\xi_2(x, y)) \\ & \quad \left. + \frac{\alpha}{\sqrt{3}} (u_r(x, y) + u_g(x, y) + u_b(x, y)) \operatorname{div} (\xi_3(x, y)) dx dy \right\}. \end{aligned}$$

By using the same argument in proof of Proposition 3.1, we further derive that the optimization approach for SV-TV(\mathbf{u}) can be applied for DTV(\mathbf{u}). The main difference between DTV(\mathbf{u}) and SV-TV(\mathbf{u}) is how to generate the orthogonal matrix \mathbf{F} and \mathbf{P} , respectively, for possible transformation used in the optimization procedure. In the next section, we will compare the numerical performance of DTV(\mathbf{u}) with that of SV-TV(\mathbf{u}) and show that the proposed SV-TV(\mathbf{u}) is better than DTV(\mathbf{u}) in terms of color image restoration.

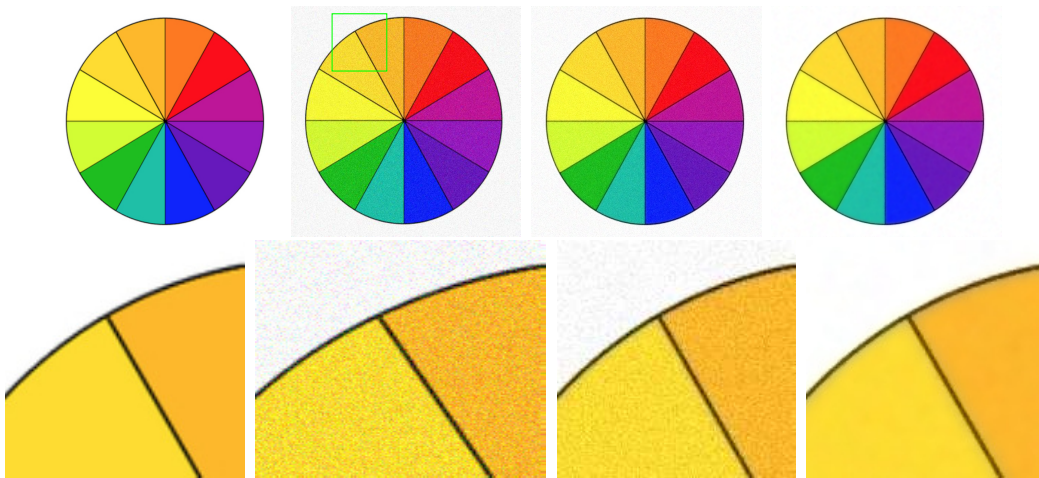


Figure 5. From left to right: clear image, noisy image, color correction by using saturation regularization, and denoised image.

5. Numerical experiments. To demonstrate the effectiveness of the proposed SV-TV color image restoration model, we present the numerical results in this section. We compare CTV₂ [6], GTV [29], VTV_{Schatten} [17], DTV [26], and the proposed SV-TV for image restoration on several testing images. The quality of the recovered images is measured by

- the SSIM index [35], which has been proven to be consistent with human eye perception,
- PSNR,
- the S-CIELAB color metric [39], which includes a spatial processing step and is useful and efficient for measuring color reproduction errors of digital images.

Since the regularization parameter is not directly comparable, we solve each restoration problem with a range of different parameters and only report the best result for each regularizer in terms of PSNR in the following evaluation. For the stopping criteria, we break the iteration when the relative error of the successive iterates is less than or equal to 1×10^{-5} for all the testing methods. We set $\beta = 0.01$ for iterations when the ADMM method is employed. The proposed main algorithm is implemented in MATLAB. All the computations are performed on a PC with an Intel(R) Core(TM) i5-3230M 2.60 GHz CPU.

5.1. Saturation regularization. In this experiment, we test the color correction effect of the saturation regularization term. The clear color image is given in Figure 5, and the noisy image is displayed on the right-hand side of the clear image. We can observe that there are significant color artifacts in the noisy image, e.g., many purple and green spots on the white background, and many red and green spots on the yellow region, and so on; see the zooming part for details. We then display the restored result by using the saturation regularization ($\alpha = 0$). We see the result that although noise is still kept, color artifacts are eliminated. It's reasonable based on our definition of the saturation regularization by coupling RGB channels together. With the help of the value regularization term ($\alpha = 0.1$), we derive the denoised and color-artifact free image in Figure 5. Note that α is set to be 0.1 in the following experiments.



Figure 6. *Ground-truth images.*

5.2. Image denoising. In this test, we make use of the images in Figure 6 taken from the Berkeley Segmentation Database5 [25] to test the proposed model for image denoising with respect to different noise levels.

We artificially add Gaussian noise of standard deviation 0.05 and 0.1 to the seven ground-truth images in each channel and compute the SSIM and PSNR values for each reconstruction by comparing it to the noise-free data. By choosing the optimal value of the regularization parameter in terms of PSNR for each testing method, we obtained the values in Table 1. Note that λ is set to be 5 and 10 corresponding to standard deviation 0.1 and 0.05, respectively, in the proposed model. We clearly observe that the proposed SV-TV model provides the best SSIM and PSNR values.

As an example of our experiment, we display some denoised results in Figures 7, 8, and 9. As expected, results by using the proposed SV-TV are significantly better than those by using other methods in visual quality especially in reducing visual color artifacts. Because there is no/less coupling of channels, CTV₂, GTV, VTV_{Schatten} are clearly worse than proposed SV-TV; see the color artifacts on the dry grass and the surface of the rock in the results. It is worth emphasizing that the ground-truth images contain different textures and colors. DTV, which has good (second best besides SV-TV) color correction performance; seems not to be good with respect to detail preservation; see the stone chair and the grass.

In Table 2, we give a comparison by using the S-CIELAB color metric based on the noise of standard deviation 0.1. We show the pixel numbers with respect to S-CIELAB errors between the ground-truth images and the restored results. Pixel numbers whose S-CIELAB errors are 5 units or larger/10 units or larger are reported in Table 2. It becomes clear that the proposed SV-TV outperforms other testing methods in terms of the S-CIELAB color metric. As an example, we display the spatial distribution of S-CIELAB errors of the restored results (Figure 7) in Figure 10, and we find that SV-TV has the smallest pixel numbers

Table 1
The values of SSIM and PSNR for the denoised images.

Figure	Std	Measure	CTV ₂	GTV	VTV _{Schatten}	DTV	SV-TV
1	0.05	SSIM	0.8838	0.8829	0.8288	0.9320	0.9442
	0.05	PSNR	28.0554	27.8590	26.8567	30.5449	31.2046
1	0.1	SSIM	0.7270	0.7231	0.6657	0.8126	0.8402
	0.1	PSNR	24.1037	24.1840	23.6985	26.1999	26.5285
2	0.05	SSIM	0.8686	0.8681	0.8179	0.9194	0.9322
	0.05	PSNR	28.4481	28.4692	27.5365	30.7457	31.1504
2	0.1	SSIM	0.7033	0.7081	0.6686	0.7947	0.8197
	0.1	PSNR	24.8456	24.7632	24.3588	26.6297	26.7677
3	0.05	SSIM	0.8677	0.8681	0.8243	0.9179	0.9292
	0.05	PSNR	28.7151	28.6544	27.8111	30.8242	31.1197
3	0.1	SSIM	0.7141	0.7140	0.6773	0.8033	0.8174
	0.1	PSNR	24.9973	24.8521	24.6021	26.7469	26.8358
4	0.05	SSIM	0.8843	0.8826	0.8625	0.9292	0.9340
	0.05	PSNR	29.3248	29.3032	28.5792	31.6060	31.8763
4	0.1	SSIM	0.7651	0.7617	0.7441	0.8383	0.8424
	0.1	PSNR	25.8304	25.8166	25.3447	27.6498	27.7075
5	0.05	SSIM	0.8600	0.8597	0.8299	0.9136	0.9226
	0.05	PSNR	29.0473	29.0273	28.2514	31.2520	31.6025
5	0.1	SSIM	0.7213	0.7215	0.6981	0.8066	0.8162
	0.1	PSNR	25.4947	25.3818	24.9670	27.3007	27.3602
6	0.05	SSIM	0.8973	0.8840	0.8806	0.9309	0.9352
	0.05	PSNR	28.1422	28.0328	27.0843	30.9376	31.3083
6	0.1	SSIM	0.7707	0.7539	0.7406	0.8410	0.8474
	0.1	PSNR	23.9839	23.7902	23.2421	26.3185	26.5064
7	0.05	SSIM	0.8761	0.8625	0.8646	0.9120	0.9131
	0.05	PSNR	29.6793	28.9777	28.8962	32.1444	32.2619
7	0.1	SSIM	0.7704	0.7463	0.7198	0.8209	0.8227
	0.1	PSNR	25.7731	25.0045	25.1214	27.8597	27.8838

whose S-CIELAB errors are 10 or larger. Meanwhile, there are 2.7% and 2.9% pixels of the SV-TV results exceeding 5 units of S-CIELAB error, while the percentage of CTV₂, GTV, VTV_{Schatten}, DTV are 14.5% and 13.8%, 15.1% and 13.8%, 19.8% and 16%, 4.5% and 3.9%, respectively. These results suggest effective and efficient denoising properties of the proposed SV-TV model.

5.3. Image deblurring. In this subsection, we test the performance of the proposed SV-TV model for nonblind image deblurring. The degraded images are simulated by convoluting the ground-truth images (in Figure 6) with a Gaussian kernel of standard deviation 1/1.5 and further adding white Gaussian noise of standard deviation 0.05. Again by selecting the optimal value of the regularization parameter for each method, we derive the SSIM and PSNR values in Table 3. Note that λ is set to be 30 in the proposed model. We find that SV-TV outperforms other testing methods in terms of the values.

As an example, we show two sets of restored results of our experiments in Figures 11, 12, and 13. The quality of the restored images can be evaluated visually besides the values. We

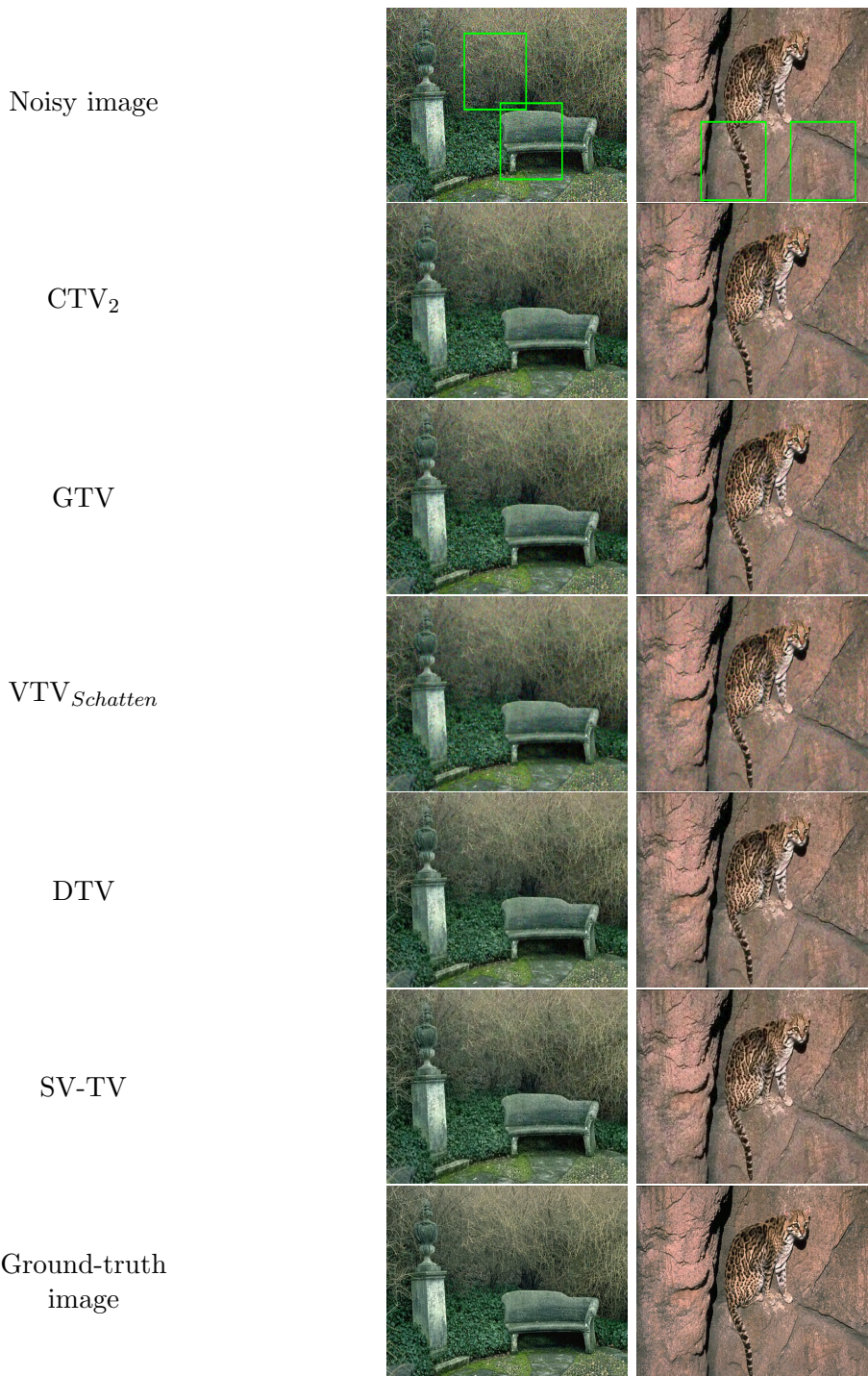


Figure 7. From top to bottom: noisy image with $\sigma = 0.1$, restored results by using CTV₂, GTV, VTV_{Schatten}, DTV, SV-TV, ground-truth image.

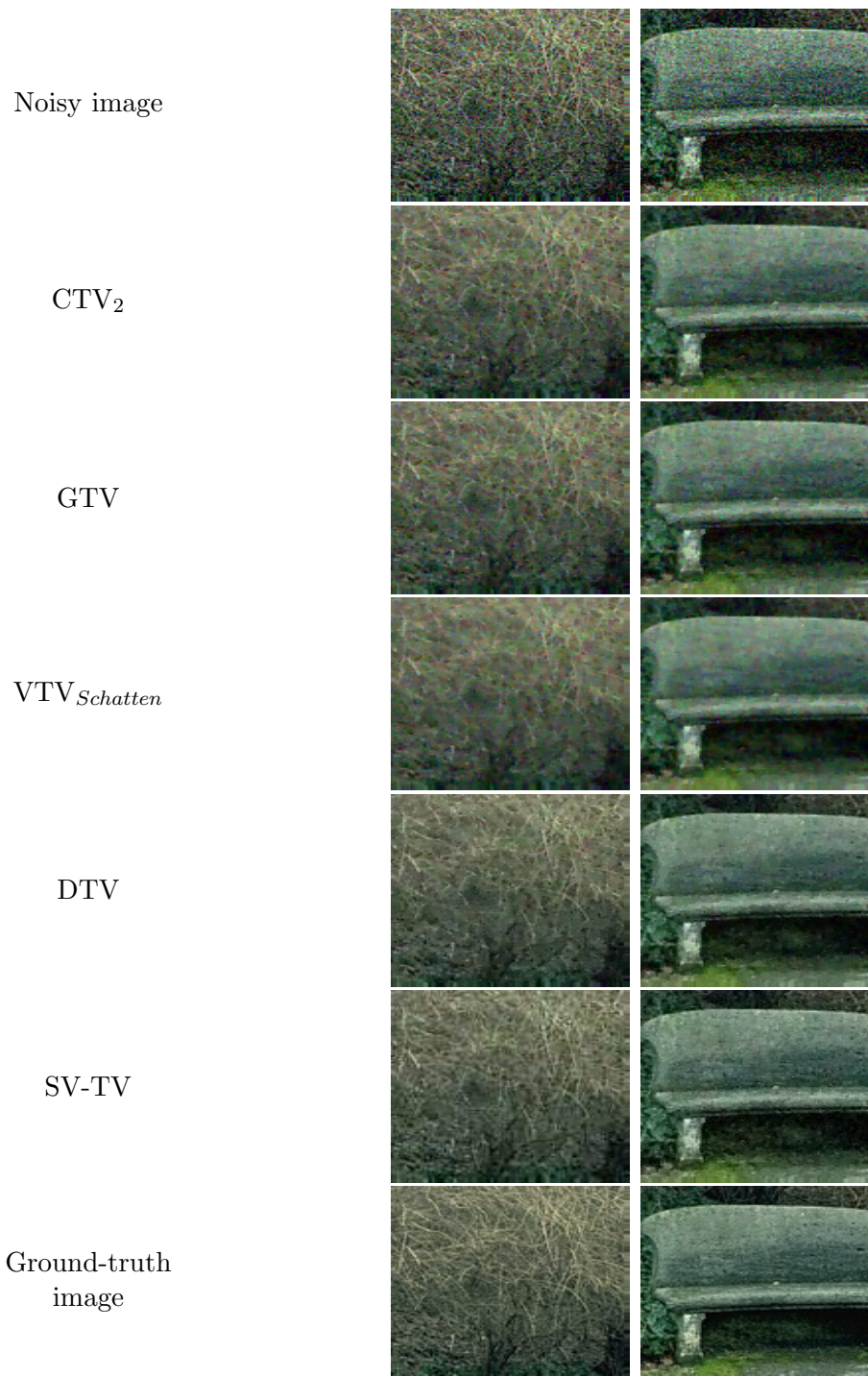


Figure 8. Corresponding zooming parts.

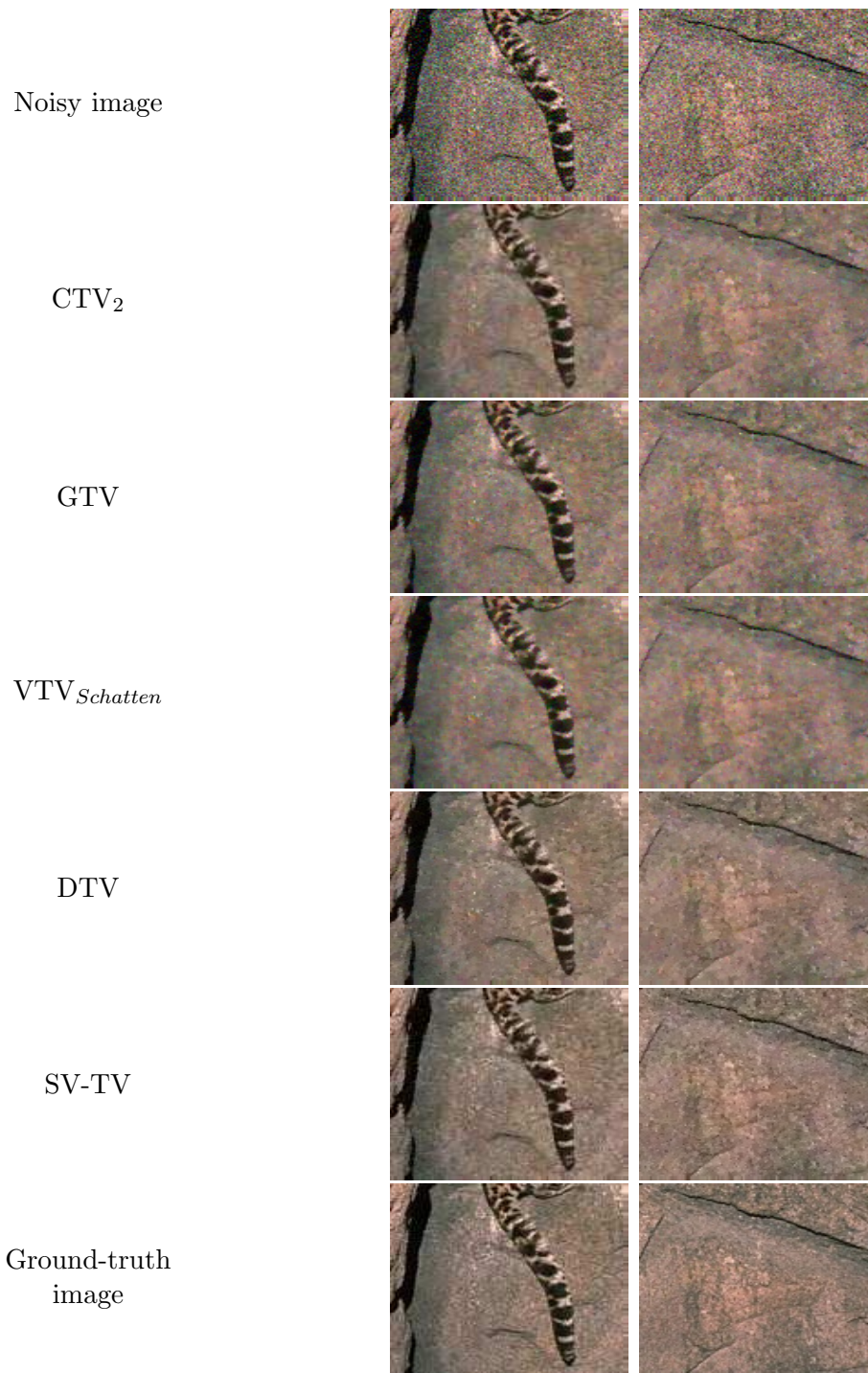


Figure 9. Corresponding zooming parts.

Table 2
Pixel numbers whose S-CIELAB errors are larger than 5, 10.

Figure	Error	CTV ₂	GTV	VTV _{Schatten}	DTV	SV-TV
1	5	20399	21301	27933	6323	3767
	10	12328	12141	13395	2797	1825
2	5	21323	21333	24616	6053	4423
	10	10816	12108	12783	2055	1465
3	5	19654	19596	26381	11269	10433
	10	11565	12186	13252	6624	6405
4	5	19974	20438	23328	5425	4297
	10	11371	11811	13706	2306	1929
5	5	18799	19256	22557	8521	7999
	10	10081	11267	12182	4620	4554
6	5	62898	65397	67962	36577	30351
	10	16327	17245	19265	4938	3389
7	5	45452	48303	52262	25023	23780
	10	8849	10667	11140	2573	2464

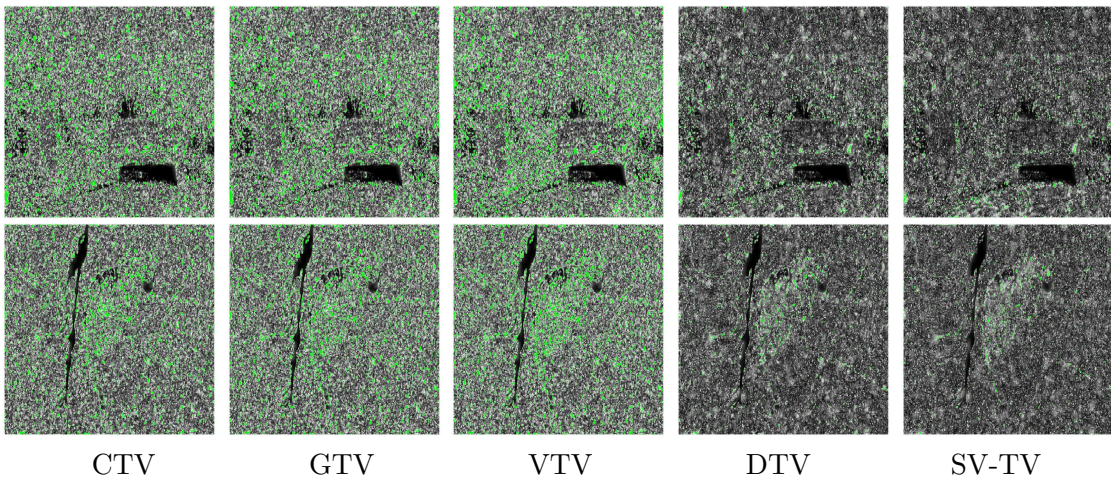


Figure 10. The spatial distribution of the S-CIELAB error (between the ground-truth and the restored result) of Figure 7. The pixel with 10 units or higher error is marked by green color. The pixel numbers are 12328, 12141, 13395, 2797, 1825 and 10816, 12108, 12783, 2055, 1465, respectively.

observe that some detailed geometry and texture can be recovered from the corrupted data by using the proposed SV-TV model, and meanwhile, color distortion has been eliminated; see the zooming parts in Figures 12 and 13. As expected, again SV-TV is superior to CTV₂, GTV, VTV_{Schatten}, DTV.

Next we consider the Gaussian kernel of standard deviation 1.5, and we show the pixel numbers with respect to S-CIELAB errors between the ground-truth images and the restored results in Table 4. Pixel numbers whose S-CIELAB errors are 10 units or larger/15 units or larger are reported. We can clearly observe that the proposed SV-TV give the best values in terms of S-CIELAB color metric. As an example, we display the spatial distribution of the

Table 3
The values of SSIM and PSNR for the restored images.

Figure	Std	Measure	CTV ₂	GTV	VTV _{Schatten}	DTV	SV-TV
1	1	SSIM	0.5716	0.5581	0.5458	0.5843	0.6252
	1	PSNR	22.4294	22.6338	22.3652	22.9966	23.1697
1	1.5	SSIM	0.4168	0.3952	0.4027	0.4485	0.4641
	1.5	PSNR	21.5337	21.5350	21.4240	21.7157	21.7720
2	1	SSIM	0.5958	0.5972	0.5854	0.6224	0.6536
	1	PSNR	23.5450	23.5350	23.2468	23.9707	24.0517
2	1.5	SSIM	0.4708	0.4542	0.4594	0.5012	0.5123
	1.5	PSNR	22.1676	22.1490	22.0262	22.3857	22.4231
3	1	SSIM	0.6189	0.6182	0.6018	0.6388	0.6716
	1	PSNR	23.8898	23.9305	23.5398	24.3279	24.4437
3	1.5	SSIM	0.4892	0.4711	0.4732	0.5171	0.5230
	1.5	PSNR	22.5032	22.5333	22.3536	22.7388	22.8130
4	1	SSIM	0.7424	0.7349	0.7125	0.7689	0.7753
	1	PSNR	25.5067	25.2550	24.7395	25.9991	26.0329
4	1.5	SSIM	0.6604	0.6593	0.6445	0.6805	0.6887
	1.5	PSNR	24.0565	24.1231	23.7860	24.2734	24.4231
5	1	SSIM	0.6538	0.6526	0.6335	0.6858	0.7018
	1	PSNR	24.1334	24.0099	23.7276	24.6343	24.7432
5	1.5	SSIM	0.5577	0.5514	0.5450	0.5845	0.5908
	1.5	PSNR	22.8366	22.7241	22.6659	23.0739	23.1302
6	1	SSIM	0.6492	0.6364	0.6277	0.6884	0.7016
	1	PSNR	20.9603	20.9143	20.6797	21.4749	21.5689
6	1.5	SSIM	0.5289	0.5138	0.5172	0.5681	0.5692
	1.5	PSNR	19.4300	19.3229	19.2889	19.6920	19.7016
7	1	SSIM	0.7186	0.6984	0.6628	0.7521	0.7542
	1	PSNR	23.5925	23.1482	23.2335	24.0762	24.1993
7	1.5	SSIM	0.6485	0.6179	0.6129	0.6403	0.6721
	1.5	PSNR	22.0125	21.5531	21.9591	22.3453	22.3522

S-CIELAB errors of the restored results (Figure 11) in Figure 14, and we find that SV-TV has the smallest pixel numbers whose S-CIELAB errors are 15 or larger. Meanwhile, There are 1.4% and 3.6% pixels of the SV-TV results exceeding 10 units, while the percentage of CTV₂, GTV, VTV_{Schatten}, DTV are 3.9% and 6%, 5% and 6.5%, 6.6% and 7%, 1.6% and 4.1%, respectively. Again these results suggest the effectiveness of the proposed SV-TV model.

6. Conclusion. As a summary, we have proposed and analyzed the SV-TV model for color image restoration. We make use of quaternion to represent color images and study the problem of color images restoration based on SV-TV. SV-TV has two parts with different faculties: one is to minimize the saturation of the gradient, and another one aims to control the smoothness of regions. This regularization may guarantee a great reduction of the unexpected chromatic intersection. Also we have studied the existence and uniqueness of the solution of the SV-TV model and present the numerical algorithms based on ADMM. Numerical results have demonstrated that the performance of the proposed model is better than other testing methods.

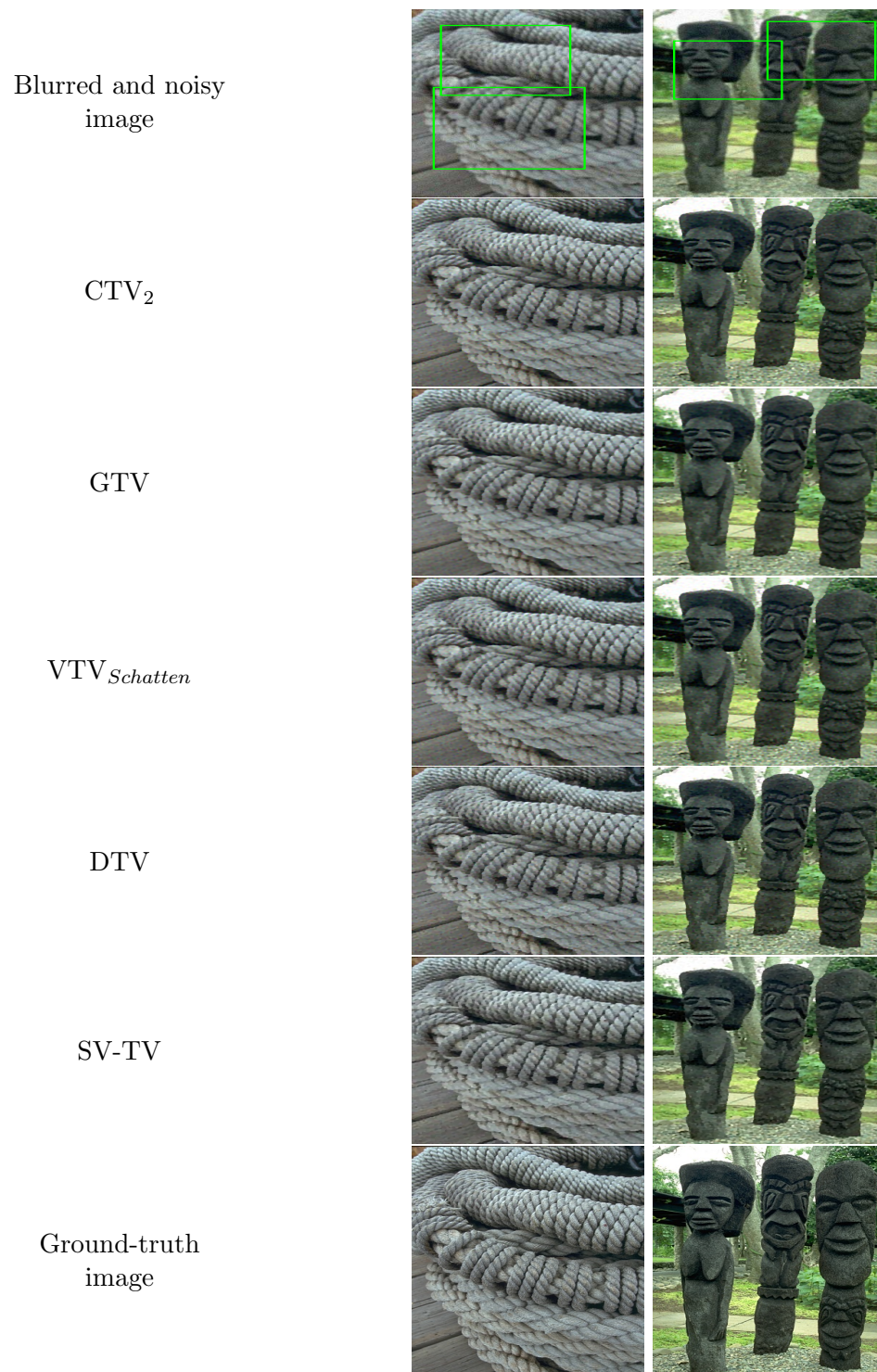


Figure 11. From top to bottom: blurred and noisy image, restored results by using CTV_2 , GTV , $\text{VTV}_{\text{Schatten}}$, DTV , SV-TV , ground-truth image.

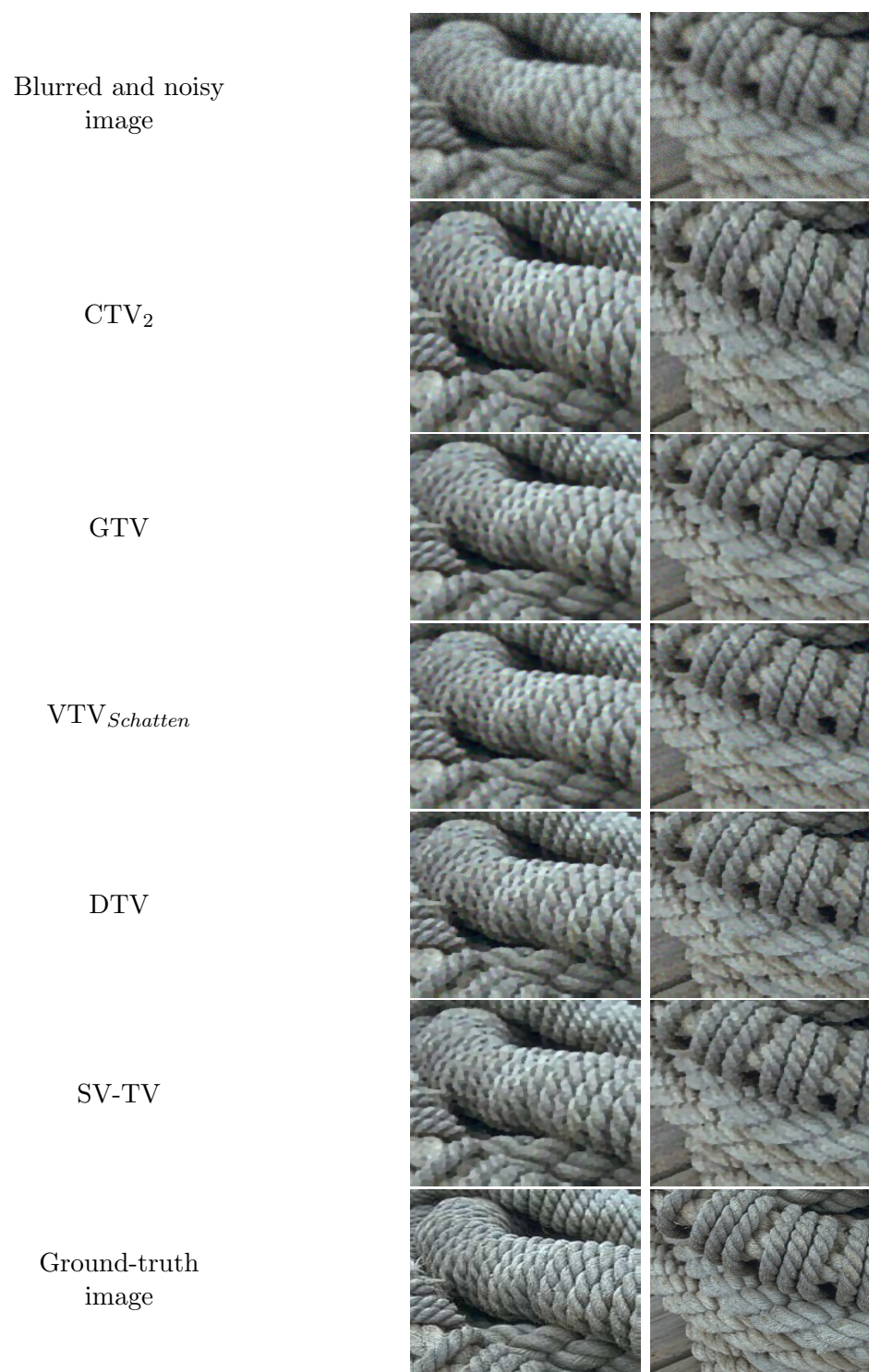


Figure 12. Corresponding zooming parts.

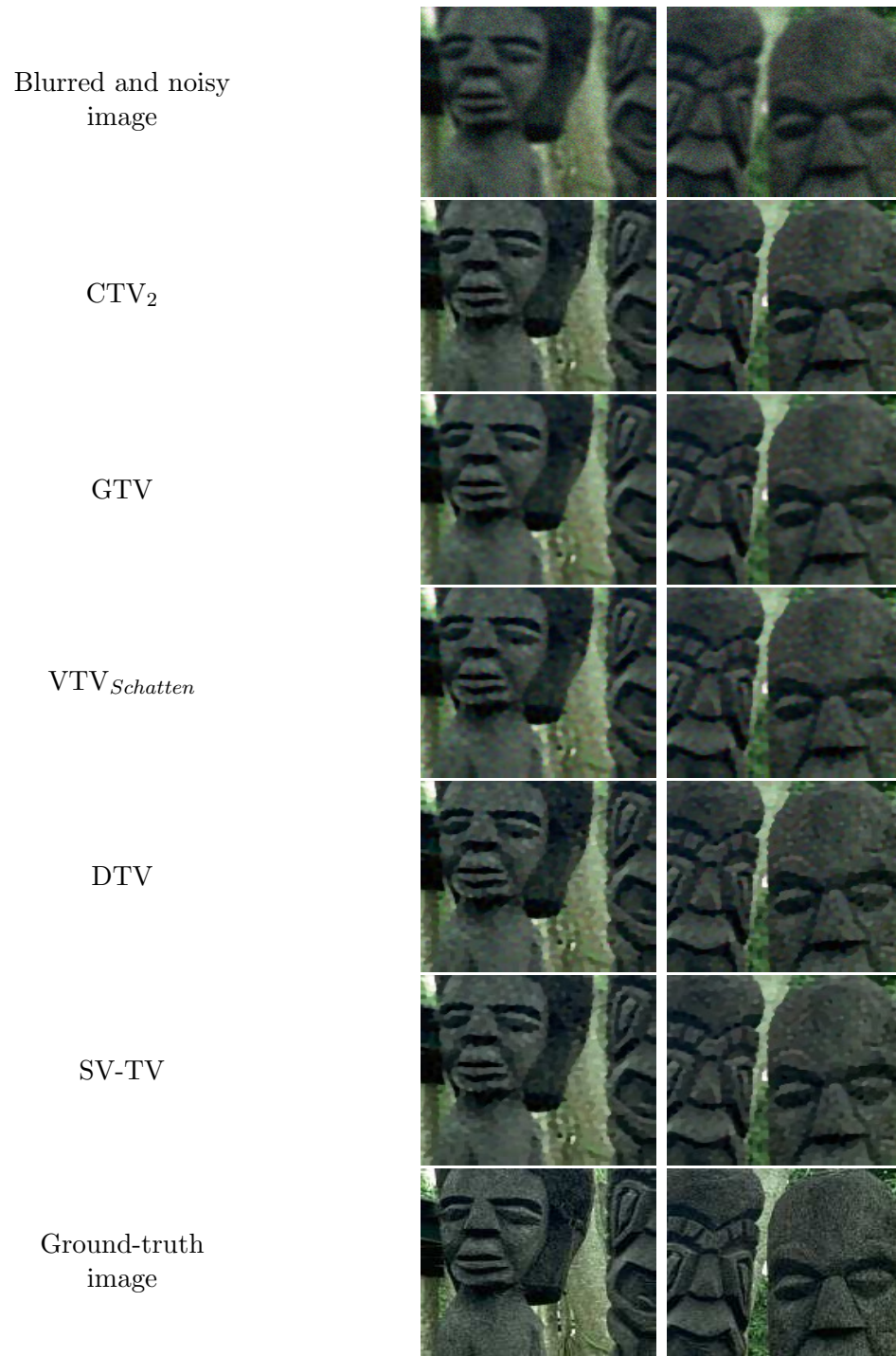


Figure 13. Corresponding zooming parts.

Table 4
Pixel numbers whose S-CIELAB errors are larger than 10, 15.

Figure	Error	CTV ₂	GTV	VTV _{Schatten}	DTV	SV-TV
1	10	12764	11702	12840	8220	6551
	15	5459	5736	5885	4292	3907
2	10	9114	9679	11224	5034	4383
	15	4839	5047	5564	3539	3257
3	10	12264	12386	13268	10354	9577
	15	7976	8334	8444	7018	6830
4	10	5960	7731	10132	2449	2123
	15	3218	3003	4232	1722	1391
5	10	9292	10046	10818	6291	5506
	15	5136	5653	5520	4055	3903
6	10	32149	33179	34196	27404	25525
	15	14884	15780	16024	12190	11552
7	10	16610	19257	19146	14031	13027
	15	6337	8196	6798	4634	4563

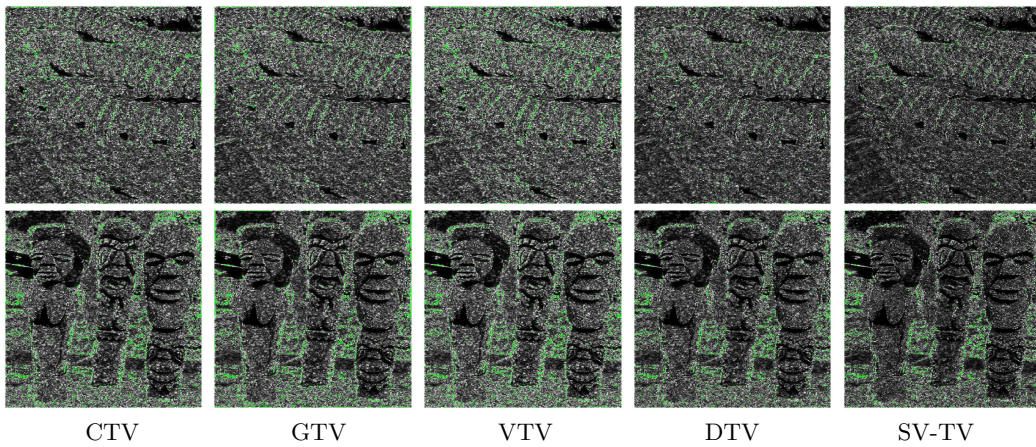


Figure 14. The spatial distribution of the S-CIELAB error of Figure 11. The pixel with 15 units or higher error is marked by green color. The pixel numbers are 3218, 3003, 4232, 1722, 1391 and 5136, 5653, 5520, 4055, 3903, respectively.

REFERENCES

- [1] H. ATTOUCH, G. BUTTAZZO, AND G. MICHAILLE, *Variational Analysis in Sobolev and BV Spaces: Applications to PDEs and Optimization*, MPS-SIAM Ser. Optim. 6, SIAM, Philadelphia, 2006.
- [2] M. BENNING, C. BRUNE, M. BURGER, AND J. MÜLLER, *Higher-order TV methods—Enhancement via Bregman iteration*, J. Sci. Comput., 54 (2013), pp. 269–310.
- [3] R. BERGMANN, R. H. CHAN, R. HIELSCHER, J. PERSCH, AND G. STEIDL, *Restoration of Manifold-Valued Images by Half-Quadratic Minimization*, arXiv:1505.07029v3, 2015.
- [4] T. BLOMGREN AND T. CHAN, *Color TV: Total variation methods for restoration of vector valued images*, IEEE Trans. Image Process., 7 (1998), pp. 304–309.

- [5] K. BREDIES, K. KUNISCH, AND T. POCK, *Total generalized variation*, SIAM J. Imaging Sci., 3 (2010), pp. 492–526.
- [6] X. BRESSON AND T. CHAN, *Fast dual minimization of the vectorial total variation norm and applications to color image processing*, Inverse Probl. Imag., 2 (2008), pp. 255–284.
- [7] A. CHAMBOLLE, *An algorithm for total variation minimization and applications*, J. Math. Imaging Vision, 20 (2004), pp. 89–97.
- [8] T. CHAN, S. KANG, AND J. SHEN, *Total variation denoising and enhancement of color images based on the CB and HSV color models*, J. Visual Commun. Image Repres., 12 (2001), pp. 422–435.
- [9] T. CHAN, A. MARQUINA, AND P. MULET, *High-order total variation-based image restoration*, SIAM J. Sci. Comput., 22 (2000), pp. 503–516.
- [10] B. COLL, J. DURAN, AND C. SBERT, *Half-linear regularization for nonconvex image restoration models*, Inverse Probl. Imag., 9 (2015), pp. 337–370.
- [11] P. DENIS, P. CARRE, AND C. FERNANDEZ-MALOIGNE, *Spatial and spectral quaternionic approaches for colour images*, Comput. Vis. Image Und., 107 (2007), pp. 74–87.
- [12] J. DURAN, M. MOELLER, C. SBERT, AND D. CREMERS, *Collaborative total variation: A general framework for vectorial TV models*, SIAM J. Imaging Sci., 9 (2016), pp. 116–151.
- [13] W. R. HAMILTON, *Elements of Quaternions*, Longmans, Green and Co., London, 1866.
- [14] T. A. ELL AND S. J. SANGWINE, *Hypercomplex Fourier transforms of color images*, IEEE Trans. Image Process., 16 (2007), pp. 22–35.
- [15] S. ESEDOGLU AND S. OSHER, *Decomposition of images by the anisotropic Rudin-Osher-Fatemi model*, Comm. Pure Appl. Math., 57 (2004), pp. 1609–1626.
- [16] G. GILBOA AND S. OSHER, *Nonlocal image regularization and supervised segmentation*, Multiscale Model. Simul., 6 (2007), pp. 595–630.
- [17] B. GOLDLUECKE, E. STREKALOVSKIY, AND D. CREMERS, *The natural vectorial total variation which arises from geometric measure theory*, SIAM J. Imaging Sci., 5 (2012), pp. 537–563.
- [18] R. C. GONZALES AND R. E. WOODS, *Digital Image Processing*, 3rd ed., Prentice Hall, Englewood Cliffs, NJ, 2008.
- [19] Z. JIA, M. NG, AND G. SONG, *A Quaternion Framework for Robust Color Images Completion*, preprint, 2018, <http://www.math.hkbu.edu.hk/~mng/QMC.pdf>
- [20] Z. JIA, M. NG, AND G. SONG, *Lanczos Method for Large-Scale Quaternion Singular Value Decomposition*, preprint, 2018, <http://www.math.hkbu.edu.hk/~mng/lanczosSVDQ.pdf>.
- [21] R. KIMMEL, R. MALLADI, AND N. SOCHEN, *Images as embedded maps and minimal surfaces: Movies, color, texture, and volumetric medical images*, Int. J. Comp. Vis., 39 (2000), pp. 111–129.
- [22] S. LEFKIMMIATIS, A. ROUSSOS, M. UNSER, AND P. MARAGOS, *Convex generalizations of total variation based on the structure tensor with applications to inverse problems*, in Scale Space and Variational Methods in Computer Vision, Lecture Notes in Comput. Sci. 7893, Springer, Berlin, 2013, pp. 48–60.
- [23] M. LYSAKER, A. LUNDERVOLD, AND X.-C. TAI, *Noise removal using fourth-order partial differential equations with applications to medical magnetic resonance images in space and time*, IEEE Trans. Image Process., 12 (2003), pp. 1579–1590.
- [24] M. LYSAKER, S. OSHER, AND X.-C. TAI, *Noise removal using smoothed normals and surface fitting*, IEEE Trans. Image Process., 13 (2004), pp. 1345–1457.
- [25] D. MARTIN, C. FOWLKES, D. TAL, AND J. MALIK, *A database of human segmented natural images and its application to evaluating segmentation algorithms and measuring ecological statistics*, in Proceedings of the IEEE International Conference on Computer Vision (ICCV), 2001, pp. 416–423.
- [26] S. ONO AND I. YAMADA, *Decorrelated vectorial total variation*, in Proceedings of the IEEE Conference on Computer Vision and Pattern Recognition (CVPR), 2014, pp. 4090–4097.
- [27] K. PAPAFITSOROS AND C.-B. SCHÖNLIEB, *A combined first and second order variational approach for image reconstruction*, J. Math. Imaging Vision, 48 (2014), pp. 308–338.
- [28] S. PEI, J. CHANG, AND J. DING, *Quaternion matrix singular value decomposition and its applications for color image processing*, in Proceedings of the IEEE International Conference on Image Processing (ICIP), 2003, pp. 805–808.
- [29] P. RODRIGUEZ AND B. WOHLBERG, *A generalized vector-valued total variation algorithm*, in Proceedings of the IEEE International Conference on Image Processing (ICIP), 2009, pp. 1309–1312.

- [30] L. RUDIN, S. OSHER, AND E. FATEMI, *Nonlinear total variation based noise removal algorithms*, Phys. D, 60 (1992), pp. 259–268.
- [31] S. J. SANGWINE, *Fourier transforms of colour images using quaternion or hypercomplex numbers*, Electron. Lett., 32 (1996), pp. 1979–1980.
- [32] S. J. SANGWINE, *Colour in image processing*, Electron. Commun. Eng. J., 12 (2000), pp. 211–219.
- [33] G. SAPIRO, *Vector-valued active contours*, in Proceedings of the IEEE Conference on Computer Vision and Pattern Recognition (CVPR), 1996, pp. 680–685.
- [34] O. N. SUBAKAN AND B. C. VEMURI, *A quaternion framework for color image smoothing and segmentation*, Int. J. Comput. Vis., 91 (2011), pp. 233–250.
- [35] Z. WANG, A. BOVIK, H. SHEIKH, AND E. P. SIMONCELLI, *Image quality assessment: From error visibility to structural similarity*, IEEE Trans. Image Process., 13 (2004), pp. 600–612.
- [36] W. WANG, F. LI, AND M. NG, *Structural similarity based nonlocal variational models for image restoration*, IEEE Trans. Image Process., to appear, <https://doi.org/10.1109/TIP.2019.2906491>.
- [37] Y. WEN, M. NG, AND Y. HUANG, *Efficient Total Variation Minimization Methods for Color Image Restoration*, IEEE Trans. Image Process., 17 (2008), pp. 2081–2088.
- [38] C. WU AND X.-C. TAI, *Augmented Lagrangian method, dual methods, and split Bregman iteration for ROF, vectorial TV, and high order models*, SIAM J. Imaging Sci., 3 (2010), pp. 300–339.
- [39] X. ZHANG AND B. A. WANDELL, *A spatial extension of CIELAB for digital color image reproduction*, in Proceedings of the SID Symposiums, 1996.